Separating and Quantifying Facility-Level Methane Emissions with Overlapping Plumes for Spaceborne Methane Monitoring

Yiguo Pang[1,2], Longfei Tian[1], Denghui Hu[1], Shuang Gao[1], and Guohua Liu[1,2]

[1]Innovation Academy for Microsatellites of Chinese Academy of Sciences, Shanghai China.
[2]University of Chinese Academy of Sciences, Beijing, China.

Correspondence: Guohua Liu (liugh@microsate.com)

Abstract. Quantifying facility-level methane emission rates using satellites with fine spatial resolution has recently gained significant attention. However, the ~~existing~~ prevailing quantification algorithms usually require the methane column plume from a ~~single~~ solitary point source as input. Such approaches are challenged with overlapping plumes from multiple point sources. To address these challenges, ~~a multi-objective heuristic optimization algorithm is introduced to perform parameter~~

5 ~~estimations for~~ an approach combining the 2D multi-source Gaussian plume model ~~, which serves as the basis for the separation method. In addition, to improve the separation performance on relatively weaker sources, we proposed a metric called local binary pattern metric (LBPM) , which is only sensitive to the sign of the gradient as a minimization objective. To verify the proposed separation~~ and the integrated mass enhancement (IME) model is proposed to separate the overlapping plume and accurately quantify emission rates. This method incorporates the heuristic optimization algorithm for parameter estimations

10 of the Gaussian plume model. To validate the proposed method, observation system simulation experiments (OSSE) of various scenarios are performed~~, where the integrated mass enhancement (IME) is selected as a representative single-source quantization method~~. The result shows that plume overlapping ~~will increase~~ exacerbates the quantifying error of ~~IME as overlapping pixels may not be attributed correctly; compared to unseparated overlapping plumes,~~ the IME method, where the quantification mean absolute percentage error (MAPE) increased from 0.15 to 0.83, and it is affected by factors such as source

15 intervals, wind direction, and interference emission rates. By contrast, the proposed separation method ~~decreases~~ mitigates this interference, reducing the quantification MAPE from ~~1.46 to~~ 0.83 to 0.38. Moreover, the proposed method also outperforms the multi-source Gaussian plume fitting, with a MAPE of 0.45~~on synthetic observation over real targets~~. Our separation method can separate the observation of overlapping plumes from multiple sources into ~~several observations~~distinct observations, each with a plume from a single source, thereby extending ~~single point~~ the more precise single-point source quantifying algorithms,

20 ~~such as IME~~the IME method, to be applicable within scenarios of ~~multiple point sources.~~ multiple-point sources. This method can help future spaceborne carbon inventorying on spatially clustering carbon-emitting facilities.

1 Introduction

Since the industrial revolution, the increasing anthropogenic emissions of greenhouse gases (GHG), have emerged as the foremost contributor to global warming and climate change, obstructing global sustainable development (IPCC, 2021). To

tackle this challenge, the global community has united and expressed a strong will to limit long-term warming below 1.5°C above the pre-industrial level, as stipulated in the Paris Agreement under the United Nations Framework Convention on Climate Change (UNFCCC). Comprehensive monitoring of global GHG is vital for verifying human activities' impacts on climate change, observing climate change trends, formulating solutions to address climate change, and evaluating the efficacy of climate policies. The conventional way to estimate GHG emissions is to multiply the elements of human activities by emission factors, using statistical methods (Calvo Buendia et al., 2019). Yet, owing to the substantial uncertainty of emission factors and source coverage (Zhao et al., 2017; Suarez et al., 2019), the performance of this bottom-up method is limited. In this regard, spaceborne GHG monitoring capabilities, e.g., OCO-2/3 (Nassar et al., 2017), TROPOMI (Zhang et al., 2020) and TanSat (Yang et al., 2023), have demonstrated their ability to quantify anthropogenic GHG emissions from large sources, such as cities and large thermal power plants, which are considered point sources. Spaceborne GHG monitoring is capable of undertaking independent, objective, and high spatiotemporal coverage measuring, and is thus considered important to verify the accuracy of bottom-up GHG emission inventories (Calvo Buendia et al., 2019; Liu et al., 2022).

Methane (CH_4) is a greenhouse gas second only to carbon dioxide(CO_2) in terms of radiative forcing, with a global warming potential (GWP-100) of about 27-29 times that of CO_2 on unit emission and a lifespan of only about 11.8 years (IPCC, 2021). As a result, taking proactive measures to reduce anthropogenic methane emissions can help alleviate global warming in the short term. Numerous studies indicate that anthropogenic methane emissions are primarily concentrated at a number of high-emission point sources (Nisbet et al., 2020; Cusworth et al., 2020; Duren et al., 2019; Frankenberg et al., 2016). Furthermore, a detected methane plume typically shows a higher signal-to-noise ratio (SNR) than CO_2 due to the significantly lower background concentration of methane (around 1.8 ppm) compared to CO_2 (approximately 420 ppm), as well as the stronger absorption cross-section of methane. These features provide convenience for spaceborne monitoring of anthropogenic methane emissions. A recent trend is monitoring methane point sources using orbital instruments with fine spatial resolution, as smaller pixels are more sensitive to column enhancement of point sources with relatively lower emissions rates (Jervis et al., 2021). For instance, GHGSat is a dedicated commercial constellation for GHG point source monitoring, with a resolution of 25–50 m (Jervis et al., 2021). Its supper fine spectral resolution endows it with a low retrieval uncertainty of 1-5% (Varon et al., 2018). Guanter et al. (2021) described detecting methane plumes with PRISMA, a versatile hyperspectral satellite. Sánchez-García et al. (2022) elucidated the detection of methane plumes with WorldView-3, a commercial multispectral satellite with a spatial resolution of 3.5 m.

One of the primary purposes of spaceborne methane point source monitoring is to quantify the emission rates. To do so, a widely used method is spaceborne measuring backscattered solar radiation in visible and shortwave infrared (VSWIR). The methane concentration (or its enhancement) is then retrieved using inversion algorithms,

Observed (or synthesized) column concentration enhancement

Our separation method
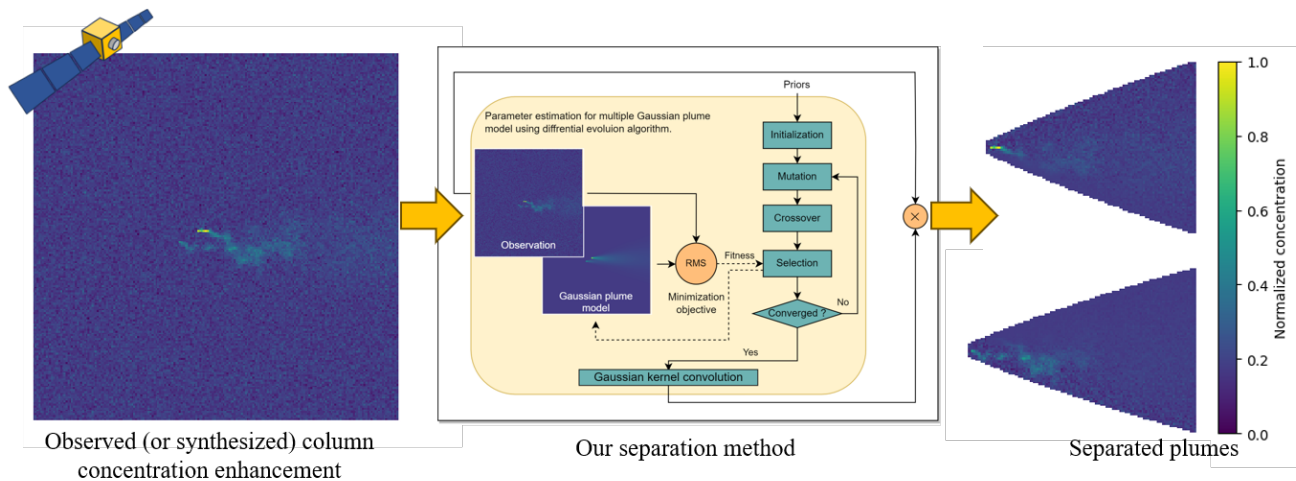
Separated plumes

Figure 1. ~~Proposed~~ The proposed methodology for separating overlapping plumes. A heuristic optimization-based method is proposed to estimate the Gaussian plume parameters for each source to separate the overlapping plumes, ~~which extends the traditional IME method to be applicable in multi-source emission scenarios~~. This method ~~takes~~ utilizes observed methane column enhancement and ~~priors~~ auxiliary data with uncertainty as inputs~~and outputs~~, yielding the enhancements of separated plumes~~for~~. The separated plumes are then quantified with the ~~following quantification~~more precise IME method respectively.

60 such as the optimal estimation ~~theory based atmospheric inversion methods (Rodgers, 2000; Frankenberg et al., 2005; Jervis et al., 2021)~~, based methods (Rodgers, 2000; Frankenberg et al., 2005; Jervis et al., 2021); data driven methods, such as matched filter (Thorpe et al., 2014) and deep learning ~~based methods (Özdemir and Koz, 2023), to retrieve the column concentration or the column enhancement of methane . Quantification methods, including~~ methods (Özdemir and Koz, 2023). The emission rates of methane point source are then estimated with quantification methods, such as Gaussian plume fitting (Bovensmann

65 et al., 2010; Nassar et al., 2017, 2021), integrated mass enhancement (IME; Frankenberg et al., 2016; Varon et al., 2018) method and ~~Cross-sectional Flux~~ cross-sectional flux (CSF; White et al.~~.;~~, 1976; Krings et al., 2011a) method~~, are then applied in conjunction with meteorological priors to estimate the emission rates of the methane point source~~. These quantification methods usually rely on the detection or masking of plumes from observations~~. To tackle this issue~~, as well as other auxiliary data, such as meteorological data. To segment the plume pixels, Bovensmann et al. (2010) estimates the XCO_2 backgrounds

70 using the entire local observations as inputs; Nassar et al. (2017) distinct the plume and the backgrounds with a 1 % density cutoff criteria; Kuhlmann et al. (2019) proposes a Z~~test~~-test based plume detection algorithm to mask pixels with statistically higher values as the inputs; Varon et al. (2018) combines Student's t~~test~~-test with computer vision (CV) based methods to detect plume pixels. Besides, deep learning methods are employed to perform quantification (Jongaramrungruang et al., 2022) or even end-to-end detection and quantification ~~(?)~~(Joyce et al., 2023).

75 However, ~~few research consider quantifying emissions~~ limited research has specifically addressed the quantification of methane emissions originating from overlapping plumes ~~of~~emitted by multiple spatially adjacent sources. Plume overlap-

ping can be not uncommon. Based on the analysis of the VISTA-CA inventory (Hopkins et al., 2019) of potential methane sources in California, US, it is found that >90% of the intervals of a source to its neighbor are less than 200 m. Upon excluding the "oil and gas well", constituting 96.5% of the total, the median and mean intervals become 496 m and 1247 m, respectively,

80   indicating a spatial clustering distribution trend, potentially resulting in overlapping plumes. Plume overlapping poses a challenge to quantification as it breaks the one-to-one correspondence between a plume pixel and a source, which means the mass in each detected plume pixel may originate from multiple sources, introducing additional errors in quantification when the mass in a conjoint pixel is attributed to any single source. ~~In many cases, plume overlap increases the difficulty of quantification (Kuhlmann et al., 2019), or even~~ Several studies have encountered the challenge of plume overlapping, which significantly

85   complicates the quantification process (Kuhlmann et al., 2019) and, in extreme cases, makes quantification impossible (Duren et al., 2019; Kuhlmann et al., 2020; Sánchez-García et al., 2022). ~~Given that the median interval distances of potential methane sources in California, US, as we analyzed using VISTA-CA inventory (Hopkins et al., 2019) are less than 200 m, respectively, plume overlap can be not uncommon. This statement can be especially valid as the plume length for a typical 30m fine resolution methane monitoring satellite is about 67-2200 m (Ayasse et al., 2019).~~ Therefore, it is necessary to separate the

90   overlapping plumes and to ~~ensure~~ establish one-to-one ~~matches~~ correspondences between plume pixels and ~~sources, in order to extend the single point source quantification algorithms to multiple sources scenarios. Nassar et al. (2021, 2017) use the Gaussian plume model to model the interference sources as background and then applies the Gaussian plume fitting to estimate the emission rate of the primary source. However, this method requires priors from inventories for interference sources, which are mostly difficult to access for facility-level methane quantification.~~ emission sources, thus enabling accurate inventorying of

95   emission rates for each individual source.

     ~~In the past, there has been extensive research on quantifying the emission rates of atmospheric pollutant sources using ground-based sensor networks (Hutchinson et al., 2017). Due to the similarities of the physical mechanism between pollutants and GHG dispersion in the atmospheric boundary layer (ABL), source term estimation methods for atmospheric pollutants dispersion have been introduced into spaceborne GHG source monitoring, e. g., the CSF method (White et al., 1976; Krings et al., 2011a)~~

100 ~~. Multiple source estimation has also been studied in this domain, e.g., Lushi and Stockie (2010) uses a Gaussian plume model to estimate~~ There have been several studies using Gaussian plume fitting to solve plume overlapping problems for spaceborne GHG monitoring. For example, Krings et al. (2011b) employed a Gauss-Newton iteration-based optimal estimation approach to infer the emission rates of ~~multiple point source pollutants by fitting sensor measurements with linear least squares. however, the high nonlinearity of the Gaussian plume model when priors, such as wind speed, wind direction,~~

105 ~~and source locations, are uncertain, may result in estimation failure. This limitation can severely impact the performance of spaceborne measurements, where obtaining accurate priors may be difficult. One solution is to use heuristics optimization algorithms, such as genetic algorithms, to fit a Gaussian plume model to sensor measurements and estimate the emission rate (Allen et al., 2007; Haupt et al., 2007). This method can simultaneously estimate these priors, making the estimation results robust to priors~~ sources with overlapping plumes; Nassar et al. (2017, 2021) employed a method of Gaussian plume

110 combinations, where the interference sources are fixed, reducing the multi-source estimation problem into a single-source estimation problem. These methods can handle the plume overlapping on a large scale. However, these methods are challenged

for facility-level monitoring, where the auxiliary information is inaccurate or even unknown. Moreover, the Gaussian plume demonstrates uncertainty with small-scale plumes (Varon et al., 2018).

To ~~quantify facility-level methane emissions with overlapping plumes~~ address these challenges, we propose an approach for
115 the separation and quantification of emission rates from overlapping plumes by incorporating the Gaussian plume method and IME method, as shown in Fig. 1~~, a heuristic optimization algorithm is introduced to estimate the parameters of the 2-dimensional (2D)~~. Firstly, To mitigate the effects of inaccurate or missing auxiliary data, we introduce a heuristics optimization algorithm to perform parameter estimation of the Gaussian plume model~~for simulated observations and then separate overlapping plumes into a set of plumes from single sources, thus expanding the applicability of the single source quantification method~~
120 ~~(e.g., the IME method) to be applicable for quantifying emission rates of overlapping plumes from multiple point sources. In addition, a local binary pattern metric (LBPM)is proposed as one of the minimization objectives for the optimization algorithm. The LBPM, only sensitive to the gradient sign of the observed concentration, along with the conventional root mean square (RMS) metric, is used for the multi-objective optimization to improve the estimation performance on sources with relatively lower emission rates.~~. This strategy is inspired by Allen et al. (2007) and Haupt et al. (2007), who utilized the genetic algorithm,
125 a subclass of heuristic optimization algorithms, to infer pollutant emission rates by estimating Gaussian plume parameters, such as source emission rate, source location and surface wind direction, using ground-based sensors. Subsequently, source parameter estimation based on heuristic optimization algorithms gained prominence in ground-based pollutant source term estimation research (Hutchinson et al., 2017). Secondly, to address the limited performance of Gaussian plume fitting at small scales, we employ the widely accepted IME method for enhanced precision in the quantification at small scales.

130 To study the impact of ~~overlap~~ overlapping on quantification and evaluate the proposed separation method, we simulate plumes using large eddy simulations ~~with~~ conducted by the Weather and Research Forecasting Model (WRF-LES; https://www. mmm.ucar.edu/models/wrf). ~~Then,~~ Subsequently, we synthesize observations of various sources, meteorological conditions, and observation characteristics ~~are synthesized~~ based on these ~~plumes. Three sets of observation system simulation experiments~~ simulated plumes. The synthesized observations comprised three scenarios of Observation System Simulation Experiments
135 (OSSE)~~were performed, including ideal single source, ideal dual sources~~, including single-source, dual-source, and real scenarios. ~~In~~ Within these experiments, ~~the improvements of the separation algorithm in missed detection and quantization error compared with the conventional single point source quantification algorithm are evaluated. Finally, we also test our method on authentic satellite observed~~ we compare the performance of the proposed method in quantification errors against conventional single-point source quantification algorithms, as well as multi-source Gaussian plume fitting. Furthermore, we validate our
140 method by applying it to a genuine satellite-observed case featuring overlapping plumes.

2 Methods

2.1 ~~Separating~~ Separation and quantification method for overlapping plumes of multiple sources

In this section, ~~the dispersion of methane emissions was modelled using a 2D multi-point~~ a separation and quantification approach is proposed to quantify facility-level methane emissions with overlapping plumes. Section 2.1.1 describes the formulation

145   of the 2-D multi-source Gaussian plume model~~(Section 2.1.1). A multi-objective heuristic optimization algorithm is introduced to separate overlapping plumes to perform parameter estimations for the dispersion model~~by minimizing the metrics between the modelled and observed column mass images (Section 2.1.2). Furthermore, to improve the estimation performance on relatively weaker sources, a metric called LBPM is proposed for the minimization (Section ??).~~ Section 2.1.2 describes the process of separating overlapping plumes using the Gaussian plume model, with parameter estimations facilitated by a

150   heuristic optimization algorithm. Section 2.1.3 describes the combination of the separation method and the IME method for the quantification.

2.1.1   2-D multi-source Gaussian ~~plumes dispersion~~ plume model

The transport mechanism of methane from point sources in the ~~ABL~~ atmospheric boundary layer (ABL) can be very complicated, as affected by multiple factors such as atmospheric turbulence, chemical reactions and terrain effects. From the per-

155   spective of mass conservation, considering wind transport, gradient diffusion, and source-sink terms, the convection-diffusion equation can be obtained to represent this mechanism, which can be written as (Stockie, 2011)

$$\frac{\partial C}{\partial t} + \nabla \cdot (C\boldsymbol{u}) = \nabla \cdot (\mathbf{K}\nabla C) + S, \tag{1}$$

where C represents the methane column mass concentration at a certain moment; t represents time; $\boldsymbol{u}$ represents the 2D field of wind velocity vectors; matrix $\mathbf{K}$ is diagonal, with its elements representing diffusion coefficients for each wind velocity

160   direction; S represents the source item.

One way to solve this partial differential equation (PDE) is the numerical method (e.g., Hosseini and Stockie, 2017)~~, however, .~~ However, the computational cost can be enormous. Analytical methods, on the other hand, simplify the problem by making assumptions, allowing for the derivation of analytical solutions to the PDE. For instance, the Gaussian plume expression of a point source can be obtained from the convection-diffusion equation by assuming that the wind speed is constant and uniform,

165   the emission rate is time-invariant and the turbulence is negligible (Sutton, 1932; Ermak, 1977; Stockie, 2011). The Gaussian plume model is widely applied to describe the pollutants, as well as the GHG dispersion in ABL, particularly in spaceborne GHG monitoring research (Bovensmann et al., 2010; Nassar et al., 2021; Jacob et al., 2022). As a result, we ~~modelled~~ model the column mass concentration(kg ~~/m²~~ m^{-2}) at the location (x, y) using a 2D Gaussian plume model for a ground-level point source, which can be written as (Sutton, 1932; Bovensmann et al., 2010)

170
$$C(x,y) = \frac{Q}{\sqrt{2\pi}\sigma_y(x)u} \exp(-\frac{1}{2}(\frac{y}{\sigma_y(x)})^2), \tag{2}$$

where the x-axis is aligned with the direction of wind speed; Q represents the emission rate (kg s^{-1}); ~~σ_x and~~ σ_y, which ~~are functions (Briggs, 1973; Griffiths, 1994) of Pasquill stability class (Pasquill, 1961), represent the diffusion coefficients down-wind and~~ is a function of wind speed in the cloud-free atmosphere (Briggs, 1973; Griffiths, 1994), represents the diffusion coefficient across-wind~~, respectively~~; u represents the horizontal wind velocity (m s^{-1}). Eq.2 then can be extended to multiple

source scenarios of N sources and is given by

$$C_N(x,y) = \sum_{n=1}^{N} C_n(x_n', y_n'), \tag{3}$$

where

$$\begin{bmatrix} x_n' \\ y_n' \end{bmatrix} = \begin{bmatrix} \cos\theta & \sin\theta \\ -\sin\theta & \cos\theta \end{bmatrix} \begin{bmatrix} x - x_n \\ y - y_n \end{bmatrix}. \tag{4}$$

Here ~~C_n~~ $C_n(x,y)$ denotes the concentration ~~increment~~ enhancement at (x,y) caused by the emission of point source n at coordinates (x_n, y_n); θ represents the wind speed angle to the x-axis in an easting/northing Cartesian coordinate system, where $0°$ ~~represents west wind, and~~ $90°$ ~~represents south wind , etc.~~ represent the eastward and northward winds, respectively. We presume uniform wind conditions for the modeled plumes, given the spatially limited extent of facility-level plumes. This method simplifies subsequent parameter estimation to improve the convergence.

2.1.2 Overlapping plume separation method based on ~~multi-objective~~ heuristic optimization

Heuristics optimization algorithms are capable of global searching in optimization and are thus widely used for solving optimization problems. Heuristics optimization algorithms have been widely used in parameter estimation of point source dispersion models (Hutchinson et al., 2017), e.g., Allen et al. (2007), Haupt et al. (2007) and Cervone et al. (2010), showing more robust performance compared to other optimization methods such as Bayesian inference (Platt and DeRiggi, 2012). The differential evolution algorithm (Storn and Price, 1997) is a heuristic optimization algorithm inspired by the evolution theory of biological species. Due to its ability to perform global optimization for systems with multiple continuous parameters, the differential evolution algorithm is thus an ideal candidate for parameter estimation of the dispersion model discussed in Section 2.1.1.

In this study, the differential evolution algorithm is selected as the estimation algorithm to iteratively minimize the metrics between the ~~modelled~~ modeled concentration image by Eq.3 and the observed concentration image, to estimate the parameters of the dispersion model.

Here, the estimating parameters consist of source locations (x_i, y_i) and emission rates Q_i of source i, the global wind angle θ and wind velocity u. For the application of the differential evolution algorithm in this paper, the searching spaces for the estimating parameters are set as follows: ~~prior ground truths~~ $\pm$ 100 m for source locations (x_i, y_i) ~~; prior ground truth~~ from their true values; $\pm$ 50% for the wind velocity from its true value, higher than the average errors of the ~~common~~ widely used reanalysis meteorological database analyzed by Varon et al. (2018) and Duren et al. (2019); ~~prior ground truth~~ $\pm$ 45° for the wind angle θ from its true value; $0 - 5000$ kg h^{-1} for emission rates Q_i, covering all methane point sources in Duren et al. (2019).

The minimization objective is another important part to apply the optimization algorithm. The most widely used minimization objective is to minimize the root mean square (RMS) metrics between ~~modelled~~ modeled and observed concentration

205   images. The RMS metric is given as

$$\mathcal{L}_{\mathrm{RMS}} = \sqrt{\sum_{i,j} \Big(I_{\mathrm{model}}(i,j) - I_{\mathrm{obs}}(i,j)\Big)^2}, \tag{5}$$

where $I_{\mathrm{model}}(i,j)$ and $I_{\mathrm{obs}}(i,j)$ represent the ~~modelled~~ modeled and observed concentration images, respectively; i and j represent the pixel indexes in row and column, respectively. ~~In addition to minimizing RMS, a shape-sensitive metric called local binary pattern metrics (LBPM, see Section ??), which is sensitive to the gradient sign, is proposed to compensate for~~

210 ~~the suboptimal performance of the RMS metric in capturing the weaker source of unbalanced multi-source scenarios during the early stage of iterations. To combine the advantages of LBPM in fitting shapes during the early iteration stages and RMS in fitting absolute values during the later iteration stages, a weighted metric is proposed for the multi-objective optimization, given by~~

$$\mathcal{L} = \mathcal{L}_{\mathrm{RMS}} + e^{\alpha \cdot t} \cdot \mathcal{L}_{\mathrm{LBPM}},$$

215 ~~where the exponential decay weight $e^{\alpha \cdot t}$ is used to leverage two metrics; α is the decay rate constant, which is set as 1.5; t represents the number of iterations.~~

    In the application of the differential evolution algorithm, the mutation strategy is set as best-guided mutation, i.e., DE2 in ~~(Storn and Price, 1997)~~ Storn and Price (1997); the number of population (NP) is set as $10 \times (N \times 3 + 2)$, where N represents the number of sources; 3 and 2 represent the numbers of parameters to be estimated for each source and entire observation,

220 respectively; The mutation constant F is set as 1 and the cross-over constant CR is set as 0.9 according to Storn and Price (1997); the relative convergence criteria is set as 10^{-3}.

    ~~The parameter estimations of the dispersion model (Eq. 3) are obtained upon the convergence of the differential algorithm. To separate the overlapping plumes , the dispersion model is firstly run with~~ Fig. 1 illustrates the framework to separate an image of overlapping plumes into distinct images, each with a solitary plume. The parameters of the Gaussian plume model are estimated

225 iteratively using the heuristic optimization algorithm described earlier, generating a series of images each with its corresponding modeled Gaussian plume. These Gaussian plumes are then utilized as weights to allocate the original observation image pixel by pixel. However, due to the ~~estimated parameter, producing a set of Gaussian plume concentration images for each source. Next, a 2D Gaussian kernel is applied to convolve these images in order to increase robustness against the deviations of observations, LES simulated transient plumes, from the stationary Gaussian plume . Finally, the convolved plumeimage for~~

230 ~~each sourceis normalized to the summation of plume images by each pixel, resulting in a probability distribution function (PDF) to separate the overlapping plumeson a per-pixel basis. The separated plume image~~ stochastic nature of the transient plume at such small scales, there can be slight misalignments between the modeled Gaussian plume and the transient plume, particularly near the source, which brings obstacles to the following allocation. To address this misalignment issue, we employ Gaussian blur (i.e., convolution with a 2D Gaussian kernel) to smooth the modeled plumes, thereby increasing robustness

235 against the deviations of the transient plume. Formally, an image with separated plume $\hat{I}_{\mathrm{obs},n}$ of source n from observation

I_{obs} is given by

$$\hat{I}_{\mathrm{obs},n} = I_{\mathrm{obs}} \cdot \frac{\hat{C}_n}{\sum_{p=1}^{N} \hat{C}_p} \frac{<C_n>}{\sum_{p=1}^{N} <C_p>}, \tag{6}$$

where $\hat{C}_n, \hat{C}_p$ represents the modelled and convolved C_n, C_p represents the modeled plume image of source n and p, respectively; $< \cdot >$ represents the Gaussian blur operation.

240 2.1.3 ~~LBPM - a shape sensitive metric for 2D images~~

~~Haupt et al. (2007) choose RMS as the minimization metric for source parameter estimation after testing several L_p-norm metrics. However, the L_p-norm metrics, including RMS (i.e. L_2-norm) metrics, are more sensitive to data with higher values. This results in a preference towards fittingpixels with higher concentration, which means that sources with higher emission rates are prioritized over weaker sources with low emission rates, resulting in unequal fitting. A metric only sensitive to pixel~~
245 ~~variation trends instead of pixel absolute values is thus required to tackle this issue.~~

~~Inspired by the local binary patterns (LBP) descriptor (Ojala et al., 2002) in the CV community, we propose the local binary patterns metric (LBPM) to evaluate the difference between modelled and observed concentration images. An LBP descriptor is a binary sequence, generated by the relative relationships between the values of a central pixel and its neighbouring pixels , to represent the local shape. The LBP descriptors are only sensitive to the relative brightness relationship between pixels,~~
250 ~~meaning they are sensitive to variation trends but robust to absolute values of pixels.~~

~~To construct the LBPM, firstly, LBP descriptors need to be generated for each pixel . Given concentration in the central pixel as g_c, with P neighbouring pixels $\{g_1, g_2, \cdots, g_P\}$, the LBP descriptor of the central pixel is constructed by (Ojala et al., 2002)~~

~~$T = \{s(g_1 - g_c), s(g_2 - g_c), \cdots, s(g_P - g_c)\},$~~

~~where the constructing function $s(x)$ is originally defined as sign function $\mathrm{sgn}(x)$, given by~~

255 ~~$\mathrm{sgn}(x) = \begin{cases} 0, & x < 0 \\ 1, & x \geq 0. \end{cases}$~~

~~Here, considering pixel value uncertainty σ (i. e., the concentration uncertainty of observation), we define the constructing function $s(x)$ by $s_\sigma(x) = \mathrm{sgn}(x - \sigma)$~~

2.1.3 Plume quantification using IME method

A transient plume may exhibit significant deviations from the Gaussian plume at small scales, leading to unstable quantification
260 with Gaussian plume fitting. In contrast, the integrated mass enhancement (IME) method demonstrate better accuracy in qunatifying small-scale transient plumes (Varon et al., 2018; Jongaramrungruang et al., 2019). Therefore, we employ the IME method for more precise quantification on the separated plumes.

~~The following shifting procedure in Ojala et al. (2002) is omitted as rotation robustness is not desired in this research. LBPM is then obtained from the LBP descriptors. Let T^p represent the pth element in an LBP sequence, $p \in [1, P]$. For 2 given LBP sequences T_a, T_b of two pixels, their LBPM is defined as their Jaccard index,~~ The emission rates estimated by IME method is given by

$$\text{LBPM}(T_a, T_b) = \frac{1}{P} \sum_{p=1}^{P} (1 - s_\sigma(|T_a^p - T_b^p|)),$$

Varon et al. (2018)

$$Q = \frac{U_{\text{eff}} \cdot \text{IME}}{L} = \frac{U_{\text{eff}} \cdot \sum_{(x,y) \in \mathbf{I}} C(x,y) A(x,y)}{\sqrt{\sum_{(x,y) \in \mathbf{I}} A(x,y)}}, \tag{7}$$

~~where T_a^p, T_b^p represent the pth element of LBP descriptors T_a and T_b, respectively. Here, P is set as 8, meaning an LBP sequence is generated with the 8 connective pixels from a centre pixel . The order of the neighbouring pixels is arbitrary yet consistent. Similarly, the LBPM between two images can also be defined as the Jaccard index of two combination sequences, each containing LPB descriptors for every pixel in its respective image, given by~~

$$\mathcal{L}_{\text{LBPM}}(I_a, I_b) = \sum_{i,j} \text{LBPM}\Big(T_a(i,j), T_b(i,j)\Big),$$

~~where $T_a(i,j)$~~ $\mathbf{I}$ represents the set of pixels identified as plume, $C(x,y)$ represents the mass enhancement of pixel (x,y), $A(x,y)$ represents the area of pixel (x,y). The effective wind speed is a logarithmic functions with linear variations to 10-m wind speed U_{10}, where the parameters are fitted using the WRF-LES simulations (Varon et al., 2018). Our fit result is $U_{\text{eff}} = 0.55 \log U_{10} + 0.62$.

The IME method requires the specification of plume pixels $\mathbf{I}$ within the observation. Similar to Varon et al. (2018), we utilize a combination of Student's t-test and ~~$T_b(i,j)$ represent the LBP sequences for pixel (i,j) in image I_a and I_b, respectively~~2D filters to detect plume pixels in the observation. However, this single-source approach tends to introduce excessive estimation when there is more than one source, thereby hindering comparative analyses between the direct application of IME without separation (denoted as UNSEP) and the proposed separation and quantification approach (denoted as SEP). To mitigate this issue, we propose a straightforward pixel attribution method to make the results of UNSEP comparable to SEP. The attribution method relies on pixel connectivity analysis, a morphological image processing technique. For a source of interest, the pixels in its nearest connected structures are attributed to the source, designated as $\mathbf{I}$, while the remaining detected plume pixels are disregarded.

2.2 Synthesized observation

2.2.1 Methane plume simulation

290 Although there have been abundant spaceborne methane observations, these observations suffer from the demerit of the lack of ~~accurate~~ priors, challenging the evaluation of proposed methods. Therefore, simulated observations are produced for evaluation. The large eddy simulation (LES), a promising methodology for solving the Navier-Stokes equation, is widely employed to simulate the dispersion in the ABL (Stoll et al., 2020), with results well agreed with observations (Rybchuk et al., 2021; Brunner et al., 2023). The LES run by WRF, a widely adopted atmospheric numerical simulation model framework, is thus a

295 preferred option for spaceborne GHG monitoring (Varon et al., 2018; Cusworth et al., 2019; Brunner et al., 2023).

WRF-LES is ~~used~~ utilized to simulate 3D volume ~~methane concentrations~~ concentration of methane (in kg m^{-3}) ~~of dispersion plumes. The dispersion is simulated by solving the advection-diffusion equation (Eq.1)~~ from a point source, where the ~~diffusion term is negligible due to the low concentration of methane in the atmosphere. The dispersion is thus can be simulated~~ methane is modeled as passive tracer ~~gas dispersion~~ (Nottrott et al., 2014). We add a trace gas dispersion function with open boundary

300 conditions by modifying the source code of the WRF 4.4 ideal LES experiment. Similar to Varon et al. (2018), methane plumes are simulated with a mean geostrophic wind of 1, 3, 5, 7 or 9 m s^{-1}; an inversion height of 500, 800 or 1100 m; a simulation region of 3.5 km x 6 km (across and along wind) with horizontal and vertical resolutions of 20 m and 10 m, respectively. The initial temperature is set as 293 K in the mixed layer, with a lapse rate of 0.12 K m^{-1} above the inversion height. The surface sensible heat flux is set as 100 W m^{-2}, respectively. The model is run for 3 hours for spin up and 2 hours for registration with

305 30 s intervals. The trace gas emission rate is set as 1kg s^{-1}. The simulated concentration is scalable with source emission rates, as simulated by passive trace gas dispersion.

The simulated 3D volume concentration snapshots are then integrated by each column weighted by column averaging kernel (Bovensmann et al., 2010; Jongaramrungruang et al., 2019). The column averaging kernel is a vector representing the vertical sensitivity distribution of the instrument and retrieval algorithm, and it is here considered to be vertically ~~uninformed~~uniform.

310 The resulting 2D column mass field is then subjected to additive Gaussian noise, considering instrument and retrieval uncertainty. The noise is given as a percentage of methane's mean dry column concentration, which is considered 1.8 ppm (i.e., ≈ 10.3 g m^{-2} at 1 atm, dry air).

2.2.2 Synthetic observations

To evaluate the possible impact of plume overlapping on quantification and the performance of the proposed separation method,

315 we performed observation system simulation experiments (OSSEs) with simulated mass columns by WRF-LES. The OSSEs are widely applied to evaluate the spaceborne GHG source detection and quantification abilities by simulating observed spectral radiations or retrieved concentrations (Bovensmann et al., 2010; Kuhlmann et al., 2019; Varon et al., 2018). OSSEs with realistic LES simulations, accounting for actual surface ~~topology~~ topography and meteorological conditions (Stoll et al., 2020), are preferable for specific source targets, however, the computational cost can be expensive, considering massive point source

320 targets with highly heterogeneous spatial and emission conditions, e.g., targets in Duren et al. (2019). One feasible approach

is to sum multiple simulated column mass images after rotations, shiftings and concentration scalings while assuming the turbulence variations ~~between multiple mass images are minor and negligiblefor quantification algorithms~~among multiple images are negligible. This approach allows for simulating sources with arbitrary emission rates, spatial and meteorological conditions, allowing much lower computation cost and thus reducing linear time complexity ($O(N)$) to nearly constant ($O(1)$) for simulating N sources when N is large enough.

To synthesize an observation with multiple sources, we establish an easting/northing Cartesian system where the x-axis points east and the y-axis points north. The field of view (FoV) is ~~a~~ square with sides at the length of 6 km and parallel to the axes, centred at $(0,0)$ of the Cartesian system. Then, ~~N of~~ the 2D column mass snapshots are randomly selected with the given wind speed and mixing depth. These snapshots are then scaled according to the emission rate of each source. Then, to rotate and shift the snapshots for an observation, we traverse all the pixels in the observation and accumulate their mapping pixels in each snapshot. For a given pixel of the observation at (x, y), the mapping pixel indexing in the nth snapshot is given by

$$
\begin{bmatrix} i' \\ j' \end{bmatrix} = \begin{bmatrix} \cos\theta & \sin\theta \\ -\sin\theta & \cos\theta \end{bmatrix} \begin{bmatrix} x - x_n \\ y - y_n \end{bmatrix} \cdot \begin{bmatrix} \frac{1}{\Delta x} \\ \frac{1}{\Delta y} \end{bmatrix} + \begin{bmatrix} I_{\text{source}} \\ J_{\text{source}} \end{bmatrix},
\tag{8}
$$

where θ represents the wind angle to a-axis; (x_n, y_n) represents the location of source n; Δx and Δy represent the horizontal resolutions in WRF-LES; $(I_{\text{source}}, J_{\text{source}})$ represent the location of the source pixel in WRF-LES. The indices (i, j) are then rounded, thus completing the nearest neighbour interpolation. Here, considering the small size of the plume and the domain, we adopt a unified wind velocity across the domain.

2.2.3 Observation scenarios

We test our separation method under three different scenarios, namely Exp1-3, each consisting of trials with various experiment settings. ~~Typical cases~~ Examples of each scenario are shown in ~~.~~ Fig. 2. Exp1, the ~~single source~~ single-source scenario, comprises a full factorial experiment of environmental factors, source factors and observation factors to evaluate the performance of quantifying methods~~on the single source~~. Exp2, the ~~dual source~~ dual-source scenario, comprises a full factorial experiment with several ~~overlapping related factors to~~ overlapping-related factors to analyze the impact of plume overlapping, as well as to evaluate the performance of separation and quantification methods. Exp3, the random source scenario, comprises a Monte Carlo test to further evaluate the separation and quantification methods.

In Exp1, a single source is placed in the centre of the simulation domain and a full factorial experiment is conducted to test the performance of the quantifying method under all combinations of ~~levels of multiple factors~~multiple-factor levels. These factors include environmental factors (mixing depth at 500, 800, and 1100 m; wind speed at 1, 3, 5, 7, 9 m s^{-1}; wind direction at 0, 45°), source factor (emission rates ranging from 100 to 2000 kg h^{-1}), and observation factors (ground pixel size ranging from 25 to 200 m; retrieval uncertainty at 1, 3, and 5%). It is noteworthy that for observation factors, ground pixel size is determined by typical point source monitoring satellites, while retrieval uncertainty is established by satellites with ultra-fine spectral resolution, such as GHGSat (Varon et al., 2018).The wind direction is defined in the Cartesian coordinate system, and the retrieval uncertainty is considered a 0-biased additive noise with standard deviation as a percentage

of methane's mean dry column mass. Each combination is repeated for 10 times. The quantification performance of Gaussian plume fitting, unseparated IME (UNSEP) and separated IME (SEP) methods are evaluated. The results are elaborated in Section 3.1. Examples of the plume image under various conditions are shown in the supplement.

In Exp2, a secondary source is introduced as an interference source to produce overlapping, as to evaluate the impact on quantification and separation. Exp2 is also a full factorial experiment, where we fix the mixing depth at 800 m, the emission rates at 200 kg h^{-1}, the ground pixel size at 25 m, and the retrieval uncertainty at 1%. The rest factors include wind speed at 1, 3, 5, 7, 9 m s^{-1}; wind direction ranging from -90 to 90°; distance between ranging from 100 to 900 m; and the emission rates ratio between the secondary and the original source (Q_2/Q_1) ranging from 0 to 5. Each combination of trials is repeated 10 times. The quantification performance of ~~single source~~ single-source Gaussian plume fitting, multi-source Gaussian plume fitting, unseparated IME and separated IME methods are evaluated. The results are elaborated in Section 3.2. The comparable results with different ground pixel size and noise settings are shown in the supplement.

In Exp3, a Monte Carlo experiment is conducted to further assess the performance of the unseparated IME and separated IME methods. For each trial, one source is randomly sampled from the AVRIS-NG observed methane source list (Duren et al., 2019) and its geolocation and emission rate is thus specified. Likewise, additional neighbouring sources within the 6 km × 6 km domain are then included in the simulation. ~~Sources~~ For simplicity, sources with emission rates lower than 25 kg h^{-1} (accounting for about 5% of the summation) are excluded from the list as they are considered too small to be accurately measured by spaceborne measurements, and their interference as background is also negelected. Additionally, we assume all the sources in the list exhibit persistence. This assumption is supported by the average confidence for persistence in the original list is 0.83. Additionally, it compensates for the manual removal of overlapping sources during the quality control phase conducted by the list maker. ~~The persistence of sources is assumed to be 1, as to demonstrate an aggressive estimate on plume overlapping~~. The wind velocity is then obtained from the fifth generation of atmospheric reanalysis of the European Centre for Medium-Range Weather Forecasts (ECMWF-ERA5; Hersbach et al., 2020). The sampling time range for loading wind velocity covers the entire local noon in 2022. The wind velocity is considered uniform across the domain and is interpolated to the observation ~~center~~ centre using 5-point inverse distance weighting such as Xu et al. (2022). To ensure that all generated source inside the domain is quantifiable, each side of the simulation frame is extended outward 2 km for a 10 km × 10 km domain. This random experiment is repeated 2000 times. The quantification ~~performance~~ performances of the unseparated IME and separated IME methods ~~is~~ are then evaluated and elaborated in Section 3.3.

~~In this study, the integrated mass enhancement (IME) method is adopted as a representative of the single source quantification methods. The emission rates estimated by IME method is given by Varon et al. (2018)~~

$$Q = \frac{U_{\text{eff}} \cdot \text{IME}}{L} = \frac{U_{\text{eff}} \cdot \sum_{(x,y) \in \mathbf{I}} C(x,y) A(x,y)}{\sqrt{\sum_{(x,y) \in \mathbf{I}} A(x,y)}},$$

~~where $\mathbf{I}$ represents the set of pixels identified as plume, $C(x,y)$ represents the mass enhancement of pixel (x,y), $A(x,y)$ represents the area of pixel (x,y). The effective wind speed is a logarithmic functions with linear variations to 10-m wind speed~~
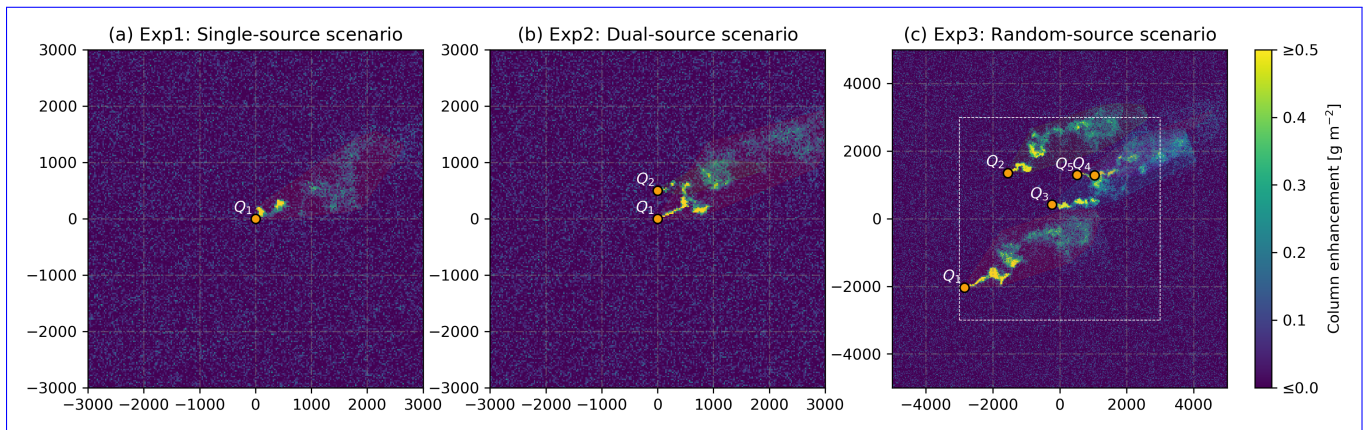
Figure 2. ~~Typical cases~~ Examples for each experiment scenario of synthesized ~~observation~~observations. The plots represent the synthesized methane column ~~observation for evaluation~~enhancement. Each semi-transparent polygon patch covers a plume, where the concentration is larger than the uncertainty. The dashed box in (c) encloses the area where random sources are generated. The emission rates vary between 200 kg h^{-1} and 2000 kg h^{-1}. In these examples, the ground pixel size is fixed at 25 m, while the retrieval uncertainty is set at 1%.

385 ~~U_{10}, where the parameters are fitted using the WRF-LES simulations (Varon et al., 2018). Our fit result is $U_{\text{eff}} = 0.55 \log U_{10} + 0.62$.~~

~~To enable the automatic application of the IME method to multi-source observations, firstly, the plume detection algorithm by Varon et al. (2018) is utilized to detect plume pixels. Then, pixel connectivity analysis, a morphological image processing technique, is applied to attribute the nearest connected structure to each source. The pixels inside these connected structures~~
390 ~~are then applied to the IME quantification.~~

2.3 EMIT observation

We also test our separation method on methane plumes retrieved by the Earth Surface Mineral Dust Source Investigation (EMIT) instrument installed on the International Space Station (ISS). The EMIT is a hyperspectral instrument capable of imaging spectroscopy in the visible to short wavelength infrared, with a nadir ground sampling distance of 30-80 m.(Green
395 et al., 2020). The methane column enhancement data ~~, labeled~~(EMITL2BCH4ENHv001) is expressed in units of parts per million meters (ppm m) and is retrieved using an adaptive matched filter technique. (Green et al., 2023b). Green et al. (2023a) also provides the corresponding identified plume complexes (EMITL2BCH4PLM v001), where the plumes sometimes overlap and thus form these clusters.

For the quantification, we first convert the concentration map from ppm m to kg m^{-2} (Sánchez-García et al., 2022).
400 Then, we applied the separation method ~~described in Section 2.1~~ to extract plumes from each source~~. The~~, and the extracted plumes are then quantified by the IME method, as described in Section 2.1. The wind velocity for separation and quantification is interpolated from ERA5 as described in Section 2.2.3. The source locations are identified through visual inspection, and cross-verified with local ground facilities using high-resolution satellite map from Google Earth. Monte

Carlo propagation is introduced to evaluate the uncertainty of the quantification ~~(Sánchez-García et al., 2022). The~~ and the systematic uncertainty of the IME method is not considered (Sánchez-García et al., 2022). For the Monte Carlo propagation, the input uncertainties include observation uncertainty from the corresponding EMITL2BCH4PLM data, and wind speed uncertainty estimated as the standard deviation of the nearest 5 points from ERA5. ~~The accuracy of IME method may also be subjected to multiple factors, including retrieval uncertainty, background, as well as the the pixel detection method (Jongaramrungruang et al., 2019; Duren et al., 2019). So the systematic errors of IME method is considered beyond the scope of this work.~~

2.4 Evaluation indicators

2.4.1 Overlapping indicator

To assess the degree of plume overlapping, a mass overlapping index is proposed, defined as the ratio of the ~~integration~~ mass integration of the interference sources to that of ~~mass contributions from the primary source and other sources to the mass of~~ the primary source~~plume~~. The mass overlapping index for source i of N sources is given by

$$\mathrm{OI}_{\mathrm{mass}_i} = \frac{\sum_{(x,y)\in \mathbf{I}}[(\sum_{n=1}^{N} C_n(x,y) - C_i(x,y)) \cdot A(x,y)]}{\sum_{(x,y)\in \mathbf{I}} C_i(x,y) A(x,y)} \tag{9}$$

where ~~I~~ $\mathbf{I}$ denotes the plume pixel of source i. Higher $\mathrm{OI}_{\mathrm{mass}_i}$ denotes that the plume of source i is subject to more severe interference.

2.4.2 Emission rates estimation indicators

The quantification of methane source is considered as solving a ~~regression~~ parameter estimation problem. So the R^2, coefficient of determination, is introduced to indicate the accuracy of overall ~~regression~~ estimation results. Furthermore, as R^2 has a relatively poor ability to explain regression results with small true values, absolute percentage error (APE) is introduced to indicate the regression error of a single sample, and mean absolute percentage error (MAPE) is introduced to indicate the overall regression error. The definitions of R^2, APE and MAPE are given by

$$R^2 = 1 - \frac{\sum_{n=1}^{N}(\hat{Q}_n - Q_n)^2}{\sum_{n=1}^{N}(\bar{Q} - Q_n)^2}, \tag{10}$$

$$\mathrm{APE}_n = \left| \frac{\hat{Q}_n - Q_n}{Q_n} \right|, \tag{11}$$

$$\mathrm{MAPE} = \frac{1}{N} \sum_{n=1}^{N} \left| \frac{\hat{Q}_n - Q_n}{Q_n} \right|, \tag{12}$$

respectively, where Q_n and $\hat{Q}_n$ represent the true emission rate and predicted emission rate, respectively, of source n; $\bar{Q}$ is the average of true emission rates; N represents the number of sources in the experiments.

3 Results

3.1 Quantification results on single source

In Exp1, we evaluate the baseline performance of various quantification methods, including the emission rates derived directly from the Gaussian plume fitting, unseparated and direct IME quantification (denoted as UNSEP), and quantification after applying the separation method ~~for single source for the extraction~~ (denoted as SEP), using a full factorial experiment.

The overall quantification errors (MAPE) for the three quantification methods are 0.89, 0.30, and 0.40, respectively. The distributions of quantification errors, in terms of absolute percentage error (APE), with respect to different simulation factors in Exp1, are shown in Fig. 3.

As shown in Fig. 3(a), the APE of all three methods exhit nearly linear incresing trends with respect to pixel size, with Pearson's correlation coefficients (R) of 0.24, 0.18 and 0.21, and all p-values are less than 0.01. Similar trends are also shown in Fig. 3(b), where the APE of three methods increase slightly with respect to uncertainty ($R = 0.16, 0.13, 0.14$; $p < 0.01$). As shown in Fig. 3(c) and Fig. 3(d), the variance of APE with respect to mixed depth and wind direction is minor. As shown in ~~Fig. 3(c) and Fig. 3(d), the variances of APEs with respect to mixed depth and wind direction are minor. As shown in 3(~~3(e), the APE of Gaussian plume and UNSEP increase with respect to the wind speed. However, the APE of the SEP reaches the maximum at the wind speed of 3 m s^{-1}. With increasing wind speed, SEP exhibits lower quantification error than UNSEP in 9 m/s. As shown in Fig. 3(f), the quantification error of all three method decrease with the emission rates, and shows a sub-linear trend.

3.2 Quantification results on dual sources

In Exp2, we introduce an interference source as to create overlapping for the full factorial experiment. After introducing an interference source, the MAPE of ~~single source~~ single-source Gaussian plume fitting increases from 0.45 to 1.23, while the increases of multi-source Gaussian plume model are negligible, which remains 0.45. Similarly, the UNSEP increases from 0.15 to 0.83, while the SEP only increases from 0.30 to 0.38.

As demonstrated in Fig. 4, the SEP shows the best quantification performance, in most cases, followed by multi-source Gaussian plume fitting, UNSEP and single-source Gaussian plume fitting, in terms of MAPE. With decreasing wind speed, the errors of quantification results by multi-source Gaussian plume fitting become comparable to that of SEP. When the wind speed is 1 m s^{-1}, the quantification results of multi-source Gaussian plume fitting ~~demonstrate slight superiority over SEP. With increasing distance and interference strength , where~~ is slight better than SEP. As distance increases or interference strength (Q_2/Q_1) decreases, plumes are less likely to overlap, ~~the performance of UNSEP begins to demonstrate superiority. When the~~
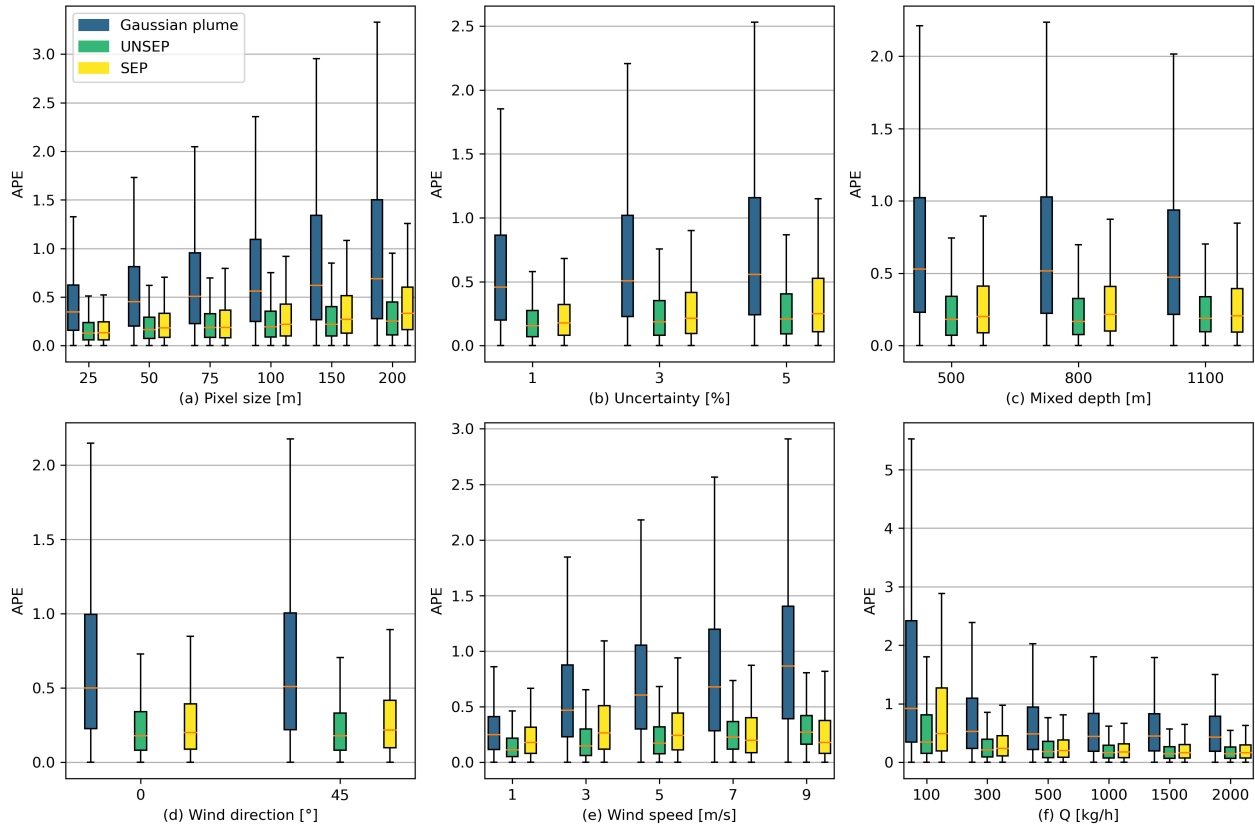
Figure 3. Distribution of quantification APE under various experimental parameters in ~~EXP1~~Exp1. The orange dashes denote the medians of APE; the boxes denote the range between the lower and upper quartiles (Q1 and Q3); ⊥ and ⊤ extend from the box by 1.5 times the inter-quartile range (IQR). The quantification errors in APE of Gaussian plume fitting, unseparated IME (UNSEP) and separated IME (SEP) methods are represented with legend.

460 ~~distance increases to~~ leading to UNSEP outperforming SEP. At 900 m ~~and the interference decreases~~ distance or interference strength decreasing to 0.5, ~~the SEP shows the~~ UNSEP achieves the best quantification performance.

~~Additionally, the~~ The multiple source Gaussian plume and SEP exhibit better quantification performance on overlapping plumes as interference strength Q_2/Q_1 intensifies. Besides, both multi-source Gaussian plume fitting and SEP show minor variations over factors including wind direction, wind speed, distance between two sources and interference strength Q_2/Q_1.

465 ~~In comparison, the quantification results of traditional~~. In contrast, single-source Gaussian plume fitting and UNSEP are more susceptible to ~~the listed factors. Their performances deteriorate~~ these factors, with their performances deteriorating as wind direction ~~aligns increasingly~~ increasingly aligns with the line connecting the ~~two sources, decreasing or increasing wind speed sources, wind speed decreases~~ (for UNSEP~~and single source~~), wind speed increases (for single-source Gaussian plume fitting~~, respectively), closer distance and stronger interference source~~), distance decreases, and interference intensifies.
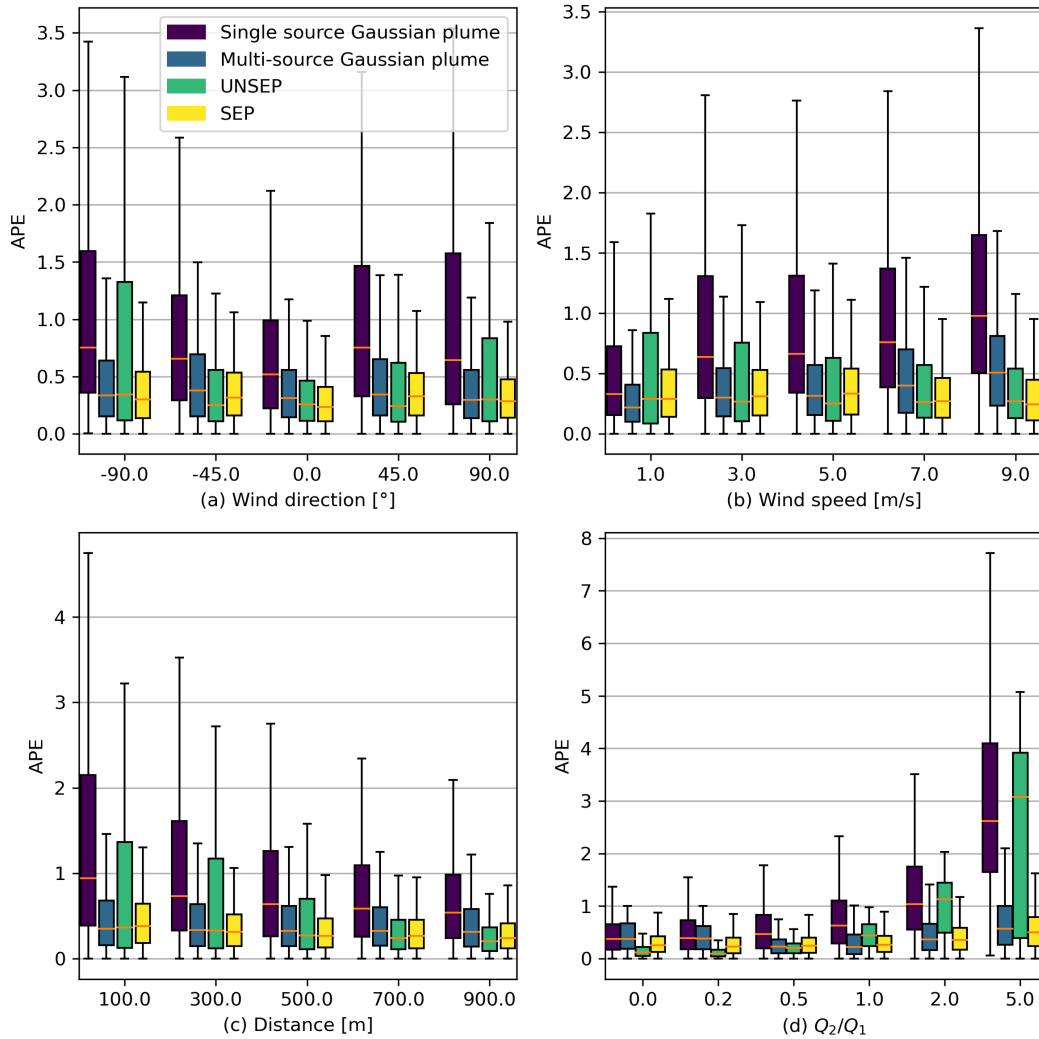
Figure 4. Distribution of quantification APE with respect to various experimental factors in ~~EXP2~~Exp2.

3.3 ~~Comparison between RMS and RMS+LBPM as the minimization objective~~

~~To evaluate the improvement of the proposed multi-objective optimization (Eq.**??**, denoted as RMS+LBPM) compared to RMS-minimizing optimization (Eq.5) on quantifying relatively weaker source, experiments are carried out based on Exp2, only appending interference strength Q_2/Q_1 with $\{10, 15, 20\}$ where higher Q_2/Q_1 means stronger interference to primary source of Q_1.~~

~~The results are shown in Table **??**, MAPEs of both methods increase with the interference strength Q_2/Q_1, and the MAPE of RMS+LBPM is lower than the MAPE of RMS for each interference strength. The APE of RMS+LBPM is significantly lower~~

3.3 Quantification results on random sources

(a) (b) (c)
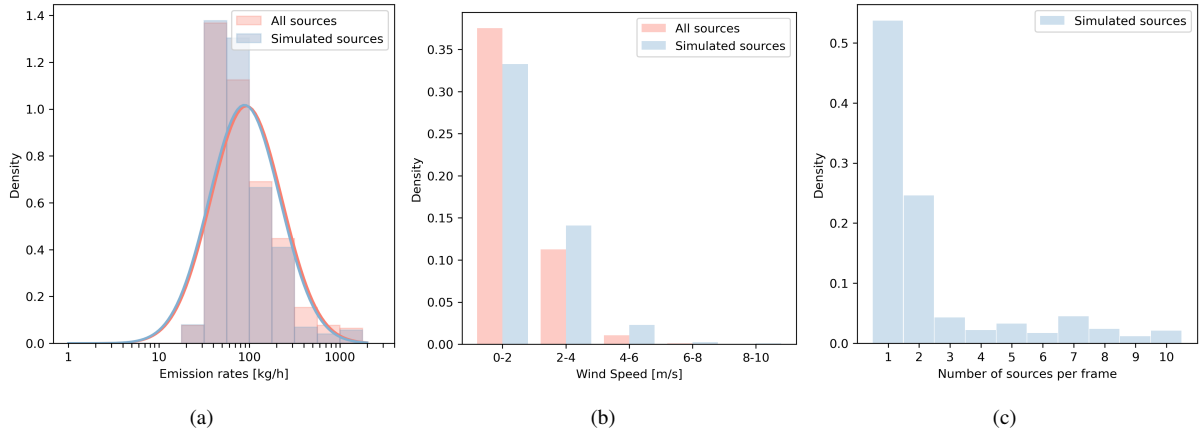
Figure 5. Statistical description of the factors in the Monte Carlo experiment (Exp3). ▮ denotes the distribution of all sources from AVIRIS-NG methane source inventory and the corresponding local noon wind speed distribution in the entire year of 2022. ▮ denotes the distribution of the selected sources in ~~EXP3~~ Exp3.

In Exp3, we focus on comparing the UNSEP and SEP in a more realistic Monte Carlo simulation. Factors including source locations, emission rates and wind velocities are randomly selected from real distributions. The sampled factors demonstrate good agreement in terms of source emission rates (Fig. 5(a)), and wind speed (Fig. 5(b)) with the real distributions of the entire source list. The sampled emission rates folow a log-normal distribution, with mean of 172.2 kg ~~s~~h^{-1} and standard deviation of 340.8 kg ~~s~~h^{-1}. As shown in Fig. 5(c), 53.7% of the frames cover one source, 24.6% of the frames cover two sources, and 21.7% of the frames cover more than two sources. On average, there are 2.33 sources per frame (6 km × 6 km).

Fig. 6 shows the quantification results of unseparated and separated IME quantifications. It is observed there is a linear underestimation for ~~UNSEP~~ SEP (Pearson's $R = 0.93$, $p < 0.01$). The SEP estimations are then corrected with regression result $y = 0.51x - 1.31$, where x represents the corrected emission rates and y represents the underestimated emission rates. After correction, the SEP shows an improvement in R^2 from 0.71 to 0.84 compared to UNSEP, and a decrease in the quantification error (MAPE) from 1.46 to 0.45. We also find that SEP is notably more accurate in estimating of low-emission sources compared to UNSEP.
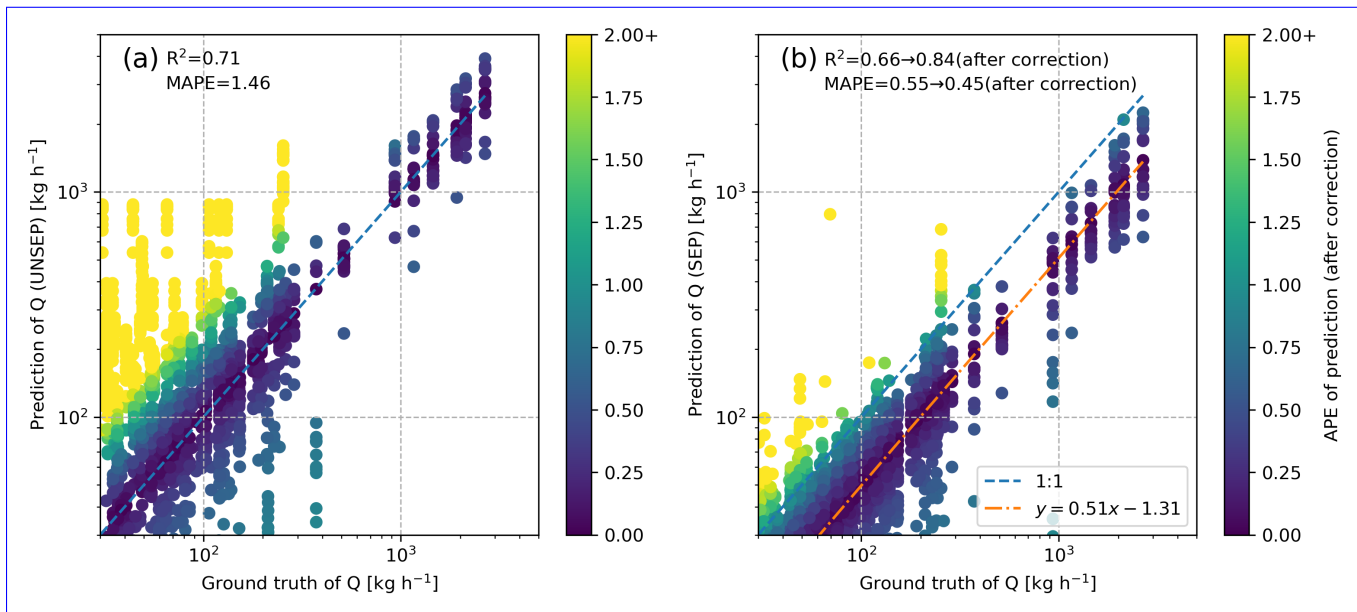
Figure 6. Comparison between quantification results of (a) unseparated quantification and (b) separated quantification in Exp3. The dash lines denote the 1:1 lines. Linear correction is applied to the SEP results in (b).

To further investigate the distribution of overlapping and the performance of UNSEP and SEP in handling overlapping, we demonstrate quantification error over the source overlapping index. The overlapping index OI_{mass} ranges from 0 to 6.09. Only 36.0% of sources are completely isolated from other sources and their overlapping index OI_{mass} is 0; half of the sources are with $OI_{mass} > 0.02$; and 4.3% of sources are be subjected to overlapping with $OI_{mass} \geq 1$. We observe a linear relation relationship between APE of UNSEP and OI_{mass} (Pearson's $R = 0.45$, $p < 0.01$), and the regression result can be expressed as $APE_{UNSEP} = 2.76 \cdot OI_{mass} + 1.34$. We define that when the APE exceeds 2 times as the intercept, the corresponding overlap situation is considered severe. Then, this results in a OI_{mass} threshold of -0.41, indicating that -18% of the sources are suffering from severe overlapping. In comparison, the corresponding OI_{mass} threshold of SEP is -16.58, indicating the effect of overlapping is largely depressed and thus results in robust quantification.

3.4 Quantification on EMIT observation

In this section, we ~~validate our separation~~ evaluate our separation and quantification method using real satellite observation of EMIT. We focus on a specified cluster of plumes observed by EMIT on 15th August 2022 at 4:28 (UTC) in Turkmenistan, near the Goturdepe oil and gas production field. The sources in this location are spatially aggregated and create significant plume overlapping (see Fig. 8). Through manual inspection and high-resolution satellite imagery verification, we identify 6 sources within the cluster. The emission rates of each source is quantified using our separated quantification method. Additionally, we
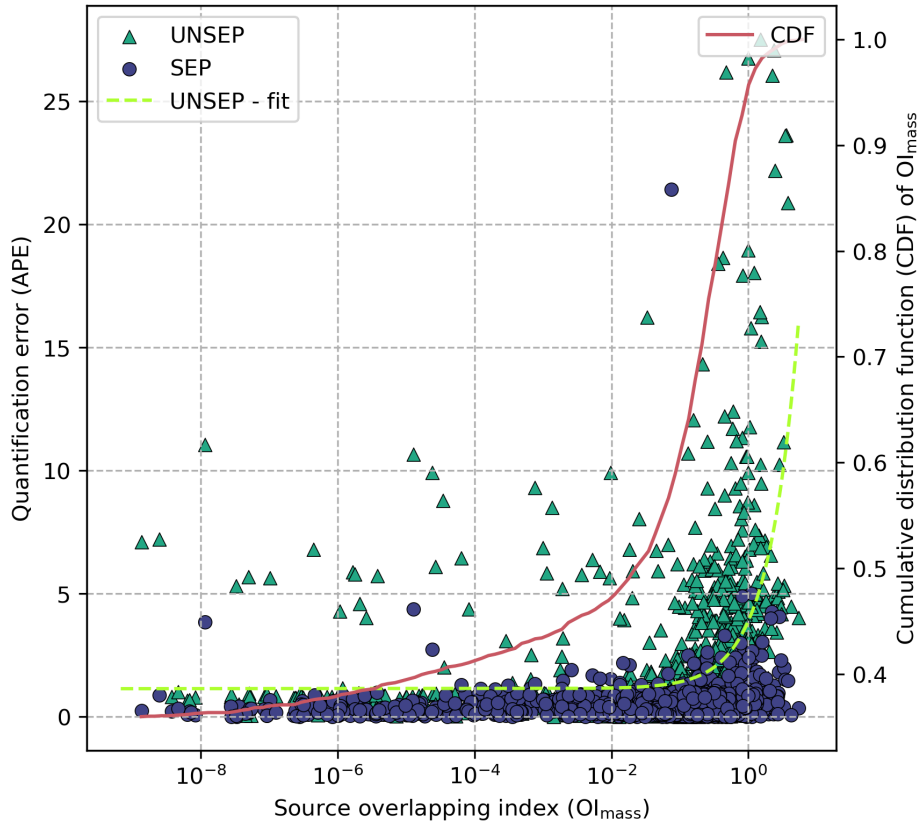
Figure 7. Comparison between quantification results and source overlapping index (OI_{mass}). The dash-line represents the linear fitted quantification error of UNSEP with respect to OI_{mass}. The red solid line represents the cumulative distribution function of OI_{mass}.

quantify the entire cluster as a whole using the conventional unseparated IME method, which does not include separation, as well as the ~~connectivity verification~~ attribution as described in Section 2.1.3.

The quantification results are shown in Table 1. The estimated emission rates for each source range from 1.64 to 5.20 t h^{-1}. We compare our estimated emission rates with previous research. We find that source Q_3 has also been quantified by Irakulis-Loitxate et al. (2022) and Sánchez-García et al. (2022) and their estimations for Q_3 are 1.4 ± 0.4 t h^{-1} and 5.0 ± 2.2 t h^{-1}, respectively. There is a gap of more than two years between these two estimations, and their estimations demonstrate significant difference. Our estimation for Q_3 on 15th August 2022 is 3.34 ± 0.90 t h^{-1}, which is comparable to the previous estimations. The summation of separated quantification results on the 6 sources is 16.77 ± 4.65 t h^{-1}. In comparison, the quantification result of the whole cluster is 21.06 ± 5.51 t h^{-1}, which is higher than the summation but ~~the~~ their difference are consistent within margins of error. It's reasonable as pixels in separated quantification may not be attributed to any source and thus excluded in the final quantification, leading to underestimations.
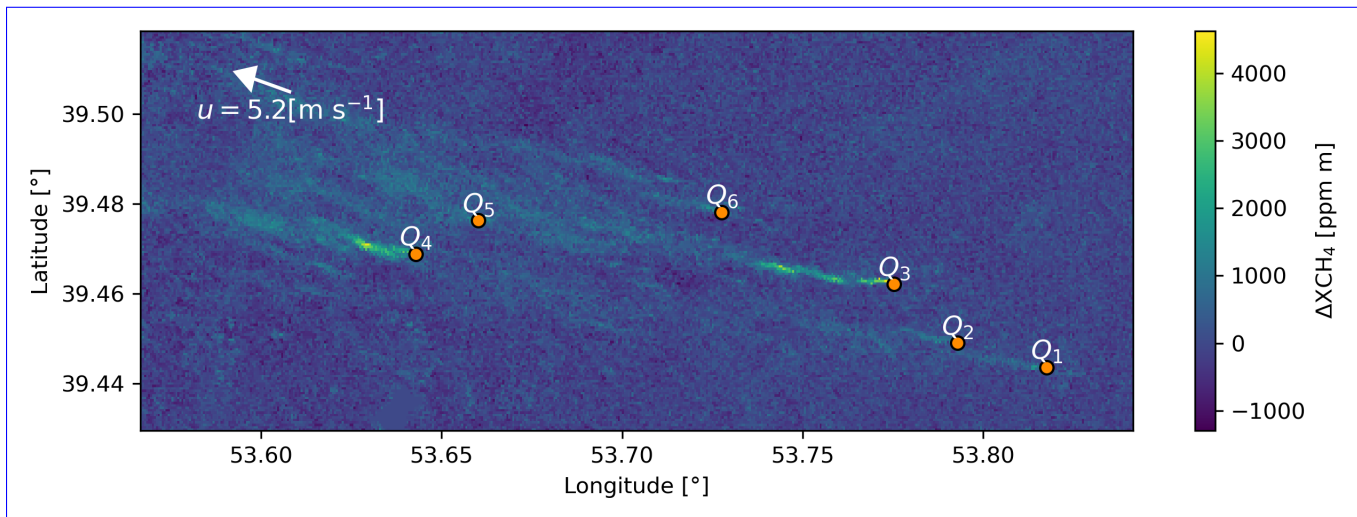
Figure 8. ~~Real satellite~~ Overlapping plumes observed ~~methane column enhancement~~ by EMIT on 15 August 2022 at 4:28 (UTC). This image is from the dataset EMITL2BCH4ENH v001, which is publicly available at https://lpdaac.usgs.gov/products/emitl2bch4enhv001/.

Table 1. Quantification results of EMIT observation. 6 sources are manually identified and quantified. The quantification results summation of separated IME method over each source separately (Summation) is compared to the results of unseparated IME method over the whole methane plume cluster (Whole).

Source ID	Source location	Estimated emission rates [t h^{-1}]	Reference emission rates [t h^{-1}]
Q_1	(39.4436°N, 53.8176°E)	1.64 ± 0.49	
Q_2	(39.4490°N, 53.7929°E)	1.35 ± 0.42	
Q_3	(39.4620°N, 53.7753°E)	3.34 ± 0.90	1.4 ± 0.4 *
			5.0 ± 2.2**
Q_4	(39.4687°N, 53.6428°E)	5.20 ± 1.38	
Q_5	(39.4762°N, 53.6602°E)	1.69 ± 0.50	
Q_6	(39.4781°N, 53.7276°E)	3.55 ± 0.95	
Summation		16.77 ± 4.65	
Whole		21.06 ± 5.51	

* Observed by PRISMA on 27 March 2020 (Irakulis-Loitxate et al., 2022).

** Observed by WorldView-3 on 10 April 2022 (Sánchez-García et al., 2022).

4 Discussion and conclusions

In this study, we ~~investigated the impact of plume overlapping on~~ compared the baseline quantification performance of the Gaussian plume model with two IME-based methods (UNSEP and SEP) for spaceborne methane point source monitoring ~~.~~ in Exp1 (see Section 3.1). Our findings indicate that the IME methods outperform the Gaussian plume model in the small scales with ground pixel sizes up to 200 m. Additionally, we observed weak positive linear relationships of the quantification error of all three methods with respect to both ground pixel size and retrieval uncertainty.

Then we investigated the impact of plume overlapping on the quantification. We found that plume overlapping increases quantification errors in Exp2~~for IME quantification, where MAPE increases~~. Specifically, the MAPE for the UNSEP method increased from 0.15 to 0.83~~compared to compared to no interference cases~~, and for single-source Gaussian plume fitting, it increased from 0.45 to 1.23 when compared to cases with no interference (see Section 3.2). Factors such as closer source intervals and disproportion emission rates will enlarge these defects. Overlapping plumes can produce connective pixels that cover multiple sources, which are ambiguous to be attributed. Simply eliminating these pixels will result in increasing missed detections and quantification errors. In addition, the relatively sparse spatial resolution of spaceborne methane monitoring techniques compared to airborne techniques can increase the proportion of these ambiguous pixels. The findings from the Monte Carlo experiment of Exp3 indicate that plume overlapping can affect up to 18% of the sources, resulting in a doubling of errors for unseparated-IME quantification (see Section 3.3). As a result, it's essential to find and attribute pixels in overlapping plumes correctly for spaceborne quantification.

To tackle this issue, we introduced a ~~multi-objective~~ heuristic optimization algorithm to perform parameter estimations for the 2D multi-source Gaussian plume model. Based on the outputs of this model with the estimated parameters, we assigned the mass to sources according to the ~~modelled~~ modeled concentrations by each pixel. In this way, we separated an overlapping-plume image into several single-plume images. This "soft segmentation" shows better performance in plume pixel detection on overlapping plumes than "hard segmentation" methods, e.g., the plume detection method by Varon et al. (2018), which assigns all the mass in a pixel to a single source while the mass may originate from multiple sources. Results in the Monte Carlo experiment (Exp3) show that the application of separation is effective in quantification, where MAPE decreases from 1.46 to 0.45, and R^2 increases from 0.71 to 0.84, compared to quantification without separation (see Section 3.3).

Additionally, our separation model can perform independent estimation for attributes such as wind speed and direction, and source locations, which make the separation robust to the ~~prior uncertainty of these factors~~uncertainty in auxiliary data. Although the emission rates as parameters of the 2D multi-source Gaussian plume model are estimated, they are only used for separation instead of quantification. As our experiment results in Exp1 and Exp2 shows, Gaussian plume fitting exhibit higher systematical uncertainty than the IME method on quantifying fine-scale methane plumes. It need to be noticed that, in our experiment, the quantification error of Gaussian plume increase with pixel size and is constantly higher than the IME methods as shown in Exp1. It is slightly different from Varon et al. (2018); Jongaramrungruang et al. (2019), which shows that plume shows better approximation of Gaussian form with increasing pixel size above 300 meters. One explaination ~~is that our WRF-LES simulation domains are samll, and such scale may not help averaging the eddies~~for the inability to pinpoint

555 the turning point of performance enhancement in Gaussian plume fitting is the limited size of our simulation domain. As we increase the pixel size, the number of pixel samples decreases, which counteracts the advantages of averaging eddies using larger pixels, thereby impeding the performance improvement of the Gaussian plume fitting. A comprehensive exploration of the trade-offs between Gaussian plume and IME methods may require large-scale, high-resolution LES simulations, and it is beyond the scope of this paper. ~~However, the Gaussian plume model is still statistically correct, which means it still can be~~
560 ~~used to perform rough estimations (e.g., Jacob et al., 2022). Acknowledging this fact, we also apply the Gaussian convolution kernel to blur the modelled plumes to increase the robustness in capturing the plume structure.~~

In the experiment on real satellite observations (see Section 3.4), firstly, we notice that identifying source locations correctly is crucial for separation and quantification. Although we verified the source with satellite imagery, it still appears less precise. Utilizing detailed facility-level inventories, such as VISTA-CA, could greatly help source detection, separation and quantifi-

565 cation. Additionally, for previously unknown emission sources, integrating multimodal information, including pipeline maps and simultaneous facility flare observations can also be introduced for accurate identifying (Irakulis-Loitxate et al., 2022). Secondly, we also notice that there are unignorable differences in source quantification results across research, as shown in Section 3.4. ~~This suggests further validation to study the systematic errors of the IME quantification method~~ The temporal variability in source emissions and the associated uncertainty in quantification are coupled, posing challenges to cross-verification among

570 observations. This suggests the need for further verification with ground truth data. Thirdly, we find that in some cases the plumes exhibit a large deviation from the WRF-LES simulation, especially in complex terrains, such as valleys. In this case, using uniform wind assumptions may also lead to the overestimation of the performance of the IME quantification method as well as the separation method.

In this study, we proposed a ~~method for separating~~ separation and quantification approach, which combines Gaussian plume

575 and IME method, to quantify the overlapping plumes from multiple facility-level point sources in spaceborne methane observations~~, thus extending the conventional single-source quantification methods to be applicable under plume-overlapping observations~~. As implied by the VISTA-CA inventory and AVIRIS-NG observed methane source list, the methane point sources can be spatially aggregated in some places, meaning that the plume overlapping may be non-negligible. This demerit will constrain the quantification scope of spaceborne GHG monitoring techniques. As a result, our separation method can be important

580 to spaceborne methane monitoring for constructing or verifying facility-level emission inventories (e.g., Duren et al., 2019), as well as environmental administration departments. For future research, a dispersion model, which is more representative of real transient plumes, can be introduced to improve the separation performance. ~~As our separation method is easily cascadable, new plume pixel detection methods can be introduced for better separation.~~ A series of tests on more realistic simulations, as well as real observations, should also be performed for further validation.

585 *Code availability.* The original version of the WRF source code is publicly available at https://www.mmm.ucar.edu/models/wrf; the source code of the proposed separation method in Section 2.1 is available upon request.

Data availability. The VISTA-CA inventory is publicly available at https://doi.org/10.3334/ORNLDAAC/1726; the AVIRIS-NG observed methane source list is publicly available as the supplementary information at https://doi.org/10.1038/s41586-019-1720-3; the ECMWF-ERA5 reanalysis meteorological data are publicly available at https://www.ecmwf.int/en/forecasts/dataset/ecmwf-reanalysis-v5; the EMIT

590 methane enhancement data are publicly available at https://lpdaac.usgs.gov/products/emitl2bch4enhv001/; the EMIT estimated methane plume complexes are publicly available at https://lpdaac.usgs.gov/products/emitl2bch4plmv001/; the LES-simulated 2D plume snapshots are available upon request.

Author contributions. YP designed and implemented the study, as well as composed the draft. GL, LT and SG conceptualized the objective of this study. DH and GL reviewed and edited the manuscript. All authors reviewed the manuscript.

595 *Competing interests.* The author has declared that there are no competing interests.

Acknowledgements. We are grateful to the affiliated group(s) at JPL for generously sharing their findings from AVIRIS-NG and EMIT. We also express our appreciation to NCAR for their efforts in the development and provision of the WRF code. Furthermore, we extend special gratitude to the two anonymous reviewers, particularly one who provided numerous practical insights and advice.

Financial support. This research has been supported by the National Key Research and Development Program of China (grant no.2022YFB3904800).

References

Allen, C. T., Haupt, S. E., and Young, G. S.: Source Characterization with a Genetic Algorithm–Coupled Dispersion–Backward Model Incorporating SCIPUFF, Journal of Applied Meteorology and Climatology, 46, 273–287, https://doi.org/10.1175/JAM2459.1, 2007.

Ayasse, A. K., Dennison, P. E., Foote, M., Thorpe, A. K., Joshi, S., Green, R. O., Duren, R. M., Thompson, D. R., and Roberts, D. A.: Methane Mapping with Future Satellite Imaging Spectrometers, Remote Sensing, 11, 3054, https://doi.org/10.3390/rs11243054, 2019.

Bovensmann, H., Buchwitz, M., Burrows, J. P., Reuter, M., Krings, T., Gerilowski, K., Schneising, O., Heymann, J., Tretner, A., and Erzinger, J.: A Remote Sensing Technique for Global Monitoring of Power Plant CO_2 Emissions from Space and Related Applications, Atmospheric Measurement Techniques, 3, 781–811, https://doi.org/10.5194/amt-3-781-2010, 2010.

Briggs, G. A.: Diffusion Estimation for Small Emissions. Preliminary Report, Tech. Rep. TID-28289, National Oceanic and Atmospheric Administration, Oak Ridge, Tenn. (USA). Atmospheric Turbulence and Diffusion Lab., https://doi.org/10.2172/5118833, 1973.

Brunner, D., Kuhlmann, G., Henne, S., Koene, E., Kern, B., Wolff, S., Voigt, C., Jöckel, P., Kiemle, C., Roiger, A., Fiehn, A., Krautwurst, S., Gerilowski, K., Bovensmann, H., Borchardt, J., Galkowski, M., Gerbig, C., Marshall, J., Klonecki, A., Prunet, P., Hanfland, R., Pattantyús-Ábrahám, M., Wyszogrodzki, A., and Fix, A.: Evaluation of Simulated CO_2 Power Plant Plumes from Six High-Resolution Atmospheric Transport Models, Atmospheric Chemistry and Physics, 23, 2699–2728, https://doi.org/10.5194/acp-23-2699-2023, 2023.

Calvo Buendia, E., Tanabe, K., Kranjc, A., Baasansuren, J., Fukuda, M., Ngarize, S., Osako, A., Pyrozhenko, Y., Shermanau, P., and Federici, S.: 2019 Refinement to the 2006 IPCC Guidelines for National Greenhouse Gas Inventories, vol. 1, Intergovernmental Panel on Climate Change, 2019.

Cervone, G., Franzese, P., and Grajdeanu, A.: Characterization of Atmospheric Contaminant Sources Using Adaptive Evolutionary Algorithms, Atmospheric Environment, 44, 3787–3796, https://doi.org/10.1016/j.atmosenv.2010.06.046, 2010.

Cusworth, D. H., Jacob, D. J., Varon, D. J., Miller, C. C., Liu, X., Chance, K., Thorpe, A. K., Duren, R. M., Miller, C. E., Thompson, D. R., Frankenberg, C., Guanter, L., and Randles, C. A.: Potential of Next-Generation Imaging Spectrometers to Detect and Quantify Methane Point Sources from Space, Atmospheric Measurement Techniques, 12, 5655–5668, https://doi.org/10.5194/amt-12-5655-2019, 2019.

Cusworth, D. H., Duren, R. M., Thorpe, A. K., Tseng, E., Thompson, D., Guha, A., Newman, S., Foster, K. T., and Miller, C. E.: Using Remote Sensing to Detect, Validate, and Quantify Methane Emissions from California Solid Waste Operations, Environmental Research Letters, 15, 054 012, https://doi.org/10.1088/1748-9326/ab7b99, 2020.

Duren, R. M., Thorpe, A. K., Foster, K. T., Rafiq, T., Hopkins, F. M., Yadav, V., Bue, B. D., Thompson, D. R., Conley, S., Colombi, N. K., Frankenberg, C., McCubbin, I. B., Eastwood, M. L., Falk, M., Herner, J. D., Croes, B. E., Green, R. O., and Miller, C. E.: California's Methane Super-Emitters, Nature, 575, 180–184, https://doi.org/10.1038/s41586-019-1720-3, 2019.

Ehret, T., De Truchis, A., Mazzolini, M., Morel, J.-M., d'Aspremont, A., Lauvaux, T., Duren, R., Cusworth, D., and Facciolo, G.: Global Tracking and Quantification of Oil and Gas Methane Emissions from Recurrent Sentinel-2 Imagery, Environmental Science & Technology, 56, 10 517–10 529, https://doi.org/10.1021/acs.est.1c08575, 2022.

Ermak, D. L.: An Analytical Model for Air Pollutant Transport and Deposition from a Point Source, Atmospheric Environment (1967), 11, 231–237, 1977.

Frankenberg, C., Platt, U., and Wagner, T.: Iterative Maximum a Posteriori (IMAP)-DOAS for Retrieval of Strongly Absorbing Trace Gases: Model Studies for CH4 and CO2 Retrieval from near Infrared Spectra of SCIAMACHY Onboard ENVISAT, Atmospheric Chemistry and Physics, 5, 9–22, https://doi.org/10.5194/acp-5-9-2005, 2005.

Frankenberg, C., Thorpe, A. K., Thompson, D. R., Hulley, G., Kort, E. A., Vance, N., Borchardt, J., Krings, T., Gerilowski, K., Sweeney, C., Conley, S., Bue, B. D., Aubrey, A. D., Hook, S., and Green, R. O.: Airborne Methane Remote Measurements Reveal Heavy-Tail Flux Distribution in Four Corners Region, Proceedings of the National Academy of Sciences of the United States of America, 113, 9734–9739, https://doi.org/10.1073/pnas.1605617113, 2016.

640 Gorroño, J., Varon, D. J., Irakulis-Loitxate, I., and Guanter, L.: Understanding the Potential of Sentinel-2 for Monitoring Methane Point Emissions, Atmospheric Measurement Techniques Discussions, pp. 1–25, https://doi.org/10.5194/amt-2022-261, 2022.

Green, R., Thorpe, A., Brodrick, P., Chadwick, D., Elder, C., Villanueva-Weeks, C., Fahlen, J., Coleman, R. W., Jensen, D., Olsen-Duvall, W., Lundeen, S., Lopez, A., and Thompson, D.: EMIT L2B Estimated Methane Plume Complexes 60 m V001, https://doi.org/10.5067/EMIT/EMITL2BCH4PLM.001, 2023a.

645 Green, R., Thorpe, A., Brodrick, P., Chadwick, D., Elder, C., Villanueva-Weeks, C., Fahlen, J., Coleman, R. W., Jensen, D., Olsen-Duvall, W., Lundeen, S., Lopez, A., and Thompson, D.: EMIT L2B Methane Enhancement Data 60 m V001, https://doi.org/10.5067/EMIT/EMITL2BCH4ENH.001, 2023b.

Green, R. O., Mahowald, N., Ung, C., Thompson, D. R., Bator, L., Bennet, M., Bernas, M., Blackway, N., Bradley, C., Cha, J., Clark, P., Clark, R., Cloud, D., Diaz, E., Ben Dor, E., Duren, R., Eastwood, M., Ehlmann, B. L., Fuentes, L., Ginoux, P., Gross, J., He, Y.,
650 Kalashnikova, O., Kert, W., Keymeulen, D., Klimesh, M., Ku, D., Kwong-Fu, H., Liggett, E., Li, L., Lundeen, S., Makowski, M. D., Mazer, A., Miller, R., Mouroulis, P., Oaida, B., Okin, G. S., Ortega, A., Oyake, A., Nguyen, H., Pace, T., Painter, T. H., Pempejian, J., Garcia-Pando, C. P., Pham, T., Phillips, B., Pollock, R., Purcell, R., Realmuto, V., Schoolcraft, J., Sen, A., Shin, S., Shaw, L., Soriano, M., Swayze, G., Thingvold, E., Vaid, A., and Zan, J.: The Earth Surface Mineral Dust Source Investigation: An Earth Science Imaging Spectroscopy Mission, in: 2020 IEEE Aerospace Conference, pp. 1–15, https://doi.org/10.1109/AERO47225.2020.9172731, 2020.

655 Griffiths, R. F.: Errors in the Use of the Briggs Parameterization for Atmospheric Dispersion Coefficients, Atmospheric Environment, 28, 2861–2865, https://doi.org/10.1016/1352-2310(94)90086-8, 1994.

Guanter, L., Irakulis-Loitxate, I., Gorrono, J., Sanchez-Garcia, E., Cusworth, D. H., Varon, D. J., Cogliati, S., and Colombo, R.: Mapping Methane Point Emissions with the PRISMA Spaceborne Imaging Spectrometer, Remote Sensing of Environment, 265, 112 671, https://doi.org/10.1016/j.rse.2021.112671, 2021.

660 Haupt, S., Young, G., and Allen, C.: A Genetic Algorithm Method to Assimilate Sensor Data for a Toxic Contaminant Release, Journal of Computers, 2, https://doi.org/10.4304/jcp.2.6.85-93, 2007.

Hersbach, H., Bell, B., Berrisford, P., Hirahara, S., Horányi, A., Muñoz-Sabater, J., Nicolas, J., Peubey, C., Radu, R., Schepers, D., Simmons, A., Soci, C., Abdalla, S., Abellan, X., Balsamo, G., Bechtold, P., Biavati, G., Bidlot, J., Bonavita, M., De Chiara, G., Dahlgren, P., Dee, D., Diamantakis, M., Dragani, R., Flemming, J., Forbes, R., Fuentes, M., Geer, A., Haimberger, L., Healy, S., Hogan, R. J.,
665 Hólm, E., Janisková, M., Keeley, S., Laloyaux, P., Lopez, P., Lupu, C., Radnoti, G., de Rosnay, P., Rozum, I., Vamborg, F., Villaume, S., and Thépaut, J.-N.: The ERA5 Global Reanalysis, Quarterly Journal of the Royal Meteorological Society, 146, 1999–2049, https://doi.org/10.1002/qj.3803, 2020.

Hopkins, F., Rafiq, T., and Duren, R.: Sources of Methane Emissions (Vista-CA), State of California, USA, https://doi.org/10.3334/ORNLDAAC/1726, 2019.

670 Hosseini, B. and Stockie, J. M.: Estimating Airborne Particulate Emissions Using a Finite-Volume Forward Solver Coupled with a Bayesian Inversion Approach, Computers & Fluids, 154, 27–43, https://doi.org/10.1016/j.compfluid.2017.05.025, 2017.

Hutchinson, M., Oh, H., and Chen, W.-H.: A Review of Source Term Estimation Methods for Atmospheric Dispersion Events Using Static or Mobile Sensors, Information Fusion, 36, 130–148, https://doi.org/10.1016/j.inffus.2016.11.010, 2017.

IPCC: Climate Change 2021: The Physical Science Basis. Contribution of Working Group I to the Sixth Assessment Report of the Intergovernmental Panel on Climate Change, vol. In Press, Cambridge University Press, Cambridge, United Kingdom and New York, NY, USA, https://doi.org/10.1017/9781009157896, 2021.

Irakulis-Loitxate, I., Guanter, L., Maasakkers, J. D., Zavala-Araiza, D., and Aben, I.: Satellites Detect Abatable Super-Emissions in One of the World's Largest Methane Hotspot Regions, Environmental Science & Technology, 56, 2143–2152, https://doi.org/10.1021/acs.est.1c04873, 2022.

Jacob, D. J., Varon, D. J., Cusworth, D. H., Dennison, P. E., Frankenberg, C., Gautam, R., Guanter, L., Kelley, J., McKeever, J., Ott, L. E., Poulter, B., Qu, Z., Thorpe, A. K., Worden, J. R., and Duren, R. M.: Quantifying Methane Emissions from the Global Scale down to Point Sources Using Satellite Observations of Atmospheric Methane, Atmospheric Chemistry and Physics, 22, 9617–9646, https://doi.org/10.5194/acp-22-9617-2022, 2022.

Jervis, D., McKeever, J., Durak, B. O. A., Sloan, J. J., Gains, D., Varon, D. J., Ramier, A., Strupler, M., and Tarrant, E.: The GHGSat-D Imaging Spectrometer, Atmospheric Measurement Techniques, 14, 2127–2140, https://doi.org/10.5194/amt-14-2127-2021, 2021.

Jongaramrungruang, S., Frankenberg, C., Matheou, G., Thorpe, A. K., Thompson, D. R., Kuai, L., and Duren, R. M.: Towards Accurate Methane Point-Source Quantification from High-Resolution 2-D Plume Imagery, Atmospheric Measurement Techniques, 12, 6667–6681, https://doi.org/10.5194/amt-12-6667-2019, 2019.

Jongaramrungruang, S., Thorpe, A. K., Matheou, G., and Frankenberg, C.: MethaNet - An AI-driven Approach to Quantifying Methane Point-Source Emission from High-Resolution 2-D Plume Imagery, Remote Sensing of Environment, 269, 112 809, https://doi.org/10.1016/j.rse.2021.112809, 2022.

Joyce, P., Ruiz Villena, C., Huang, Y., Webb, A., Gloor, M., Wagner, F. H., Chipperfield, M. P., Barrio Guilló, R., Wilson, C., and Boesch, H.: Using a Deep Neural Network to Detect Methane Point Sources and Quantify Emissions from PRISMA Hyperspectral Satellite Images, Atmospheric Measurement Techniques, 16, 2627–2640, https://doi.org/10.5194/amt-16-2627-2023, 2023.

Krings, T., Gerilowski, K., Buchwitz, M., Reuter, M., Tretner, A., Erzinger, J., Heinze, D., Pflüger, U., Burrows, J. P., and Bovensmann, H.: MAMAP – a New Spectrometer System for Column-Averaged Methane and Carbon Dioxide Observations from Aircraft: Instrument Description and Performance Analysis, Atmospheric Measurement Techniques, 4, 1735–1758, https://doi.org/10.5194/amt-4-1735-2011, 2011a.

Krings, T., Gerilowski, K., Buchwitz, M., Reuter, M., Tretner, A., Erzinger, J., Heinze, D., Pflüger, U., Burrows, J. P., and Bovensmann, H.: MAMAP – a New Spectrometer System for Column-Averaged Methane and Carbon Dioxide Observations from Aircraft: Retrieval Algorithm and First Inversions for Point Source Emission Rates, Atmospheric Measurement Techniques, 4, 1735–1758, https://doi.org/10.5194/amt-4-1735-2011, 2011b.

Kuhlmann, G., Broquet, G., Marshall, J., Clément, V., Löscher, A., Meijer, Y., and Brunner, D.: Detectability of CO_2 Emission Plumes of Cities and Power Plants with the Copernicus Anthropogenic CO_2 Monitoring (CO2M) Mission, Atmospheric Measurement Techniques, 12, 6695–6719, https://doi.org/10.5194/amt-12-6695-2019, 2019.

Kuhlmann, G., Brunner, D., Broquet, G., and Meijer, Y.: Quantifying CO2 Emissions of a City with the Copernicus Anthropogenic CO2 Monitoring Satellite Mission, Atmospheric Measurement Techniques, 13, 6733–6754, https://doi.org/10.5194/amt-13-6733-2020, 2020.

Liu, L., Chen, L., Liu, Y., Yang, D., Zhang, X., Lu, N., Ju, W., Jiang, F., Yin, Z., Liu, G., Tian, L., Hu, D., Mao, H., Liu, S., Zhang, J., Lei, L., Fan, M., Zhang, Y., Zhou, X., and Wu, Y.: Satellite Remote Sensing for Global Stocktaking: Methods, Progress and Perspectives, National Remote Sensing Bulletin, 26, 243–267, https://doi.org/10.11834/jrs.20221806, 2022.

Lushi, E. and Stockie, J. M.: An Inverse Gaussian Plume Approach for Estimating Atmospheric Pollutant Emissions from Multiple Point Sources, Atmospheric Environment, 44, 1097–1107, https://doi.org/10.1016/j.atmosenv.2009.11.039, 2010.

Nassar, R., Hill, T. G., McLinden, C. A., Wunch, D., Jones, D. B. A., and Crisp, D.: Quantifying CO2 Emissions From Individual Power Plants From Space, Geophysical Research Letters, 44, 10 045–10 053, https://doi.org/10.1002/2017GL074702, 2017.

715 Nassar, R., Mastrogiacomo, J.-P., Bateman-Hemphill, W., McCracken, C., MacDonald, C. G., Hill, T., O'Dell, C. W., Kiel, M., and Crisp, D.: Advances in Quantifying Power Plant CO2 Emissions with OCO-2, Remote Sensing of Environment, 264, 112 579, https://doi.org/10.1016/j.rse.2021.112579, 2021.

Nisbet, E. G., Fisher, R. E., Lowry, D., France, J. L., Allen, G., Bakkaloglu, S., Broderick, T. J., Cain, M., Coleman, M., Fernandez, J., Forster, G., Griffiths, P. T., Iverach, C. P., Kelly, B. F. J., Manning, M. R., Nisbet-Jones, P. B. R., Pyle, J. A., Townsend-Small, A., al-Shalaan,
720 A., Warwick, N., and Zazzeri, G.: Methane Mitigation: Methods to Reduce Emissions, on the Path to the Paris Agreement, Reviews of Geophysics, 58, e2019RG000 675, https://doi.org/10.1029/2019RG000675, 2020.

Nottrott, A., Kleissl, J., and Keeling, R.: Modeling Passive Scalar Dispersion in the Atmospheric Boundary Layer with WRF Large-Eddy Simulation, Atmospheric Environment, 82, 172–182, https://doi.org/10.1016/j.atmosenv.2013.10.026, 2014.

Ojala, T., Pietikainen, M., and Maenpaa, T.: Multiresolution Gray-Scale and Rotation Invariant Texture Classification with Local Binary
725 Patterns, IEEE Transactions on Pattern Analysis and Machine Intelligence, 24, 971–987, https://doi.org/10.1109/TPAMI.2002.1017623, 2002.

Özdemir, O. B. and Koz, A.: 3D-CNN and Autoencoder-Based Gas Detection in Hyperspectral Images, IEEE Journal of Selected Topics in Applied Earth Observations and Remote Sensing, 16, 1474–1482, https://doi.org/10.1109/JSTARS.2023.3235781, 2023.

Pasquill, F.: The Estimation of the Dispersion of Windborne Material, Australian Meteorological Magazine, pp. 33–49, 1961.

730 Platt, N. and DeRiggi, D.: Comparative Investigation of Source Term Estimation Algorithms Using FUSION Field Trial 2007 Data: Linear Regression Analysis, International Journal of Environment and Pollution, 48, 13–21, https://doi.org/10.1504/IJEP.2012.049647, 2012.

Rodgers, C. D.: Inverse Methods for Atmospheric Sounding: Theory and Practice, vol. 2 of *Series on Atmospheric, Oceanic and Planetary Physics*, WORLD SCIENTIFIC, https://doi.org/10.1142/3171, 2000.

Rybchuk, A., Alden, C. B., Lundquist, J. K., and Rieker, G. B.: A Statistical Evaluation of WRF-LES Trace Gas Dispersion Using Project
735 Prairie Grass Measurements, Monthly Weather Review, 149, 1619–1633, https://doi.org/10.1175/MWR-D-20-0233.1, 2021.

Sánchez-García, E., Gorroño, J., Irakulis-Loitxate, I., Varon, D. J., and Guanter, L.: Mapping Methane Plumes at Very High Spatial Resolution with the WorldView-3 Satellite, Atmospheric Measurement Techniques, 15, 1657–1674, https://doi.org/10.5194/amt-15-1657-2022, 2022.

Stockie, J. M.: The Mathematics of Atmospheric Dispersion Modeling, Siam Review, 53, 349–372, https://doi.org/10.1137/10080991X, 2011.

740 Stoll, R., Gibbs, J. A., Salesky, S. T., Anderson, W., and Calaf, M.: Large-Eddy Simulation of the Atmospheric Boundary Layer, Boundary-Layer Meteorology, 177, 541–581, https://doi.org/10.1007/s10546-020-00556-3, 2020.

Storn, R. and Price, K.: Differential Evolution - A Simple and Efficient Heuristic for Global Optimization over Continuous Spaces, Journal of Global Optimization, 11, 341–359, https://doi.org/10.1023/A:1008202821328, 1997.

Suarez, D. R., Rozendaal, D. M. A., De Sy, V., Phillips, O. L., Alvarez-Davila, E., Anderson-Teixeira, K., Araujo-Murakami, A., Arroyo,
745 L., Baker, T. R., Bongers, F., Brienen, R. J. W., Carter, S., Cook-Patton, S. C., Feldpausch, T. R., Griscom, B. W., Harris, N., Herault, B., Honorio Coronado, E. N., Leavitt, S. M., Lewis, S. L., Marimon, B. S., Monteagudo Mendoza, A., N'dja, J. K., N'Guessan, A. E., Poorter, L., Qie, L., Rutishauser, E., Sist, P., Sonke, B., Sullivan, M. J. P., Vilanova, E., Wang, M. M. H., Martius, C., and Herold, M.:

Estimating Aboveground Net Biomass Change for Tropical and Subtropical Forests: Refinement of IPCC Default Rates Using Forest Plot Data, Global Change Biology, 25, 3609–3624, https://doi.org/10.1111/gcb.14767, 2019.

750 Sutton, O. G.: A Theory of Eddy Diffusion in the Atmosphere, Proceedings of the Royal Society of London, Series A„ 135, 143–165, 1932.

Thorpe, A. K., Frankenberg, C., and Roberts, D. A.: Retrieval Techniques for Airborne Imaging of Methane Concentrations Using High Spatial and Moderate Spectral Resolution: Application to AVIRIS, Atmospheric Measurement Techniques, 7, 491–506, https://doi.org/10.5194/amt-7-491-2014, 2014.

Varon, D. J., Jacob, D. J., McKeever, J., Jervis, D., Durak, B. O. A., Xia, Y., and Huang, Y.: Quantifying Methane Point Sources

755 from Fine-Scale Satellite Observations of Atmospheric Methane Plumes, Atmospheric Measurement Techniques, 11, 5673–5686, https://doi.org/10.5194/amt-11-5673-2018, 2018.

Varon, D. J., McKeever, J., Jervis, D., Maasakkers, J. D., Pandey, S., Houweling, S., Aben, I., Scarpelli, T., and Jacob, D. J.: Satellite Discovery of Anomalously Large Methane Point Sources From Oil/Gas Production, Geophysical Research Letters, 46, 13 507–13 516, https://doi.org/10.1029/2019GL083798, 2019.

760 White, W., Anderson, J., Blumenthal, D., Husar, R., Gillani, N., Husar, J., and Wilson, W.: Formation and Transport of Secondary Air-Pollutants - Ozone and Aerosols in St-Louis Urban Plume, Science, 194, 187–189, https://doi.org/10.1126/science.959846, 1976.

Xu, J., Ma, Z., Yan, S., and Peng, J.: Do ERA5 and ERA5-land Precipitation Estimates Outperform Satellite-Based Precipitation Products? A Comprehensive Comparison between State-of-the-Art Model-Based and Satellite-Based Precipitation Products over Mainland China, Journal of Hydrology, 605, 127 353, https://doi.org/10.1016/j.jhydrol.2021.127353, 2022.

765 Yang, D., Hakkarainen, J., Liu, Y., Ialongo, I., Cai, Z., and Tamminen, J.: Detection of Anthropogenic CO_2 Emission Signatures with TanSat CO_2 and with Copernicus Sentinel-5 Precursor (S5P) NO_2 Measurements: First Results, Advances in Atmospheric Sciences, 40, 1–5, https://doi.org/10.1007/s00376-022-2237-5, 2023.

Zhang, Y., Gautam, R., Pandey, S., Omara, M., Maasakkers, J. D., Sadavarte, P., Lyon, D., Nesser, H., Sulprizio, M. P., Varon, D. J., Zhang, R., Houweling, S., Zavala-Araiza, D., Alvarez, R. A., Lorente, A., Hamburg, S. P., Aben, I., and Jacob, D. J.: Quantify-

770 ing Methane Emissions from the Largest Oil-Producing Basin in the United States from Space, Science Advances, 6, eaaz5120, https://doi.org/10.1126/sciadv.aaz5120, 2020.

Zhang, Z., Sherwin, E. D., Varon, D. J., and Brandt, A. R.: Detecting and Quantifying Methane Emissions from Oil and Gas Production: Algorithm Development with Ground-Truth Calibration Based on Sentinel-2 Satellite Imagery, Atmospheric Measurement Techniques, 15, 7155–7169, https://doi.org/10.5194/amt-15-7155-2022, 2022.

775 Zhao, Y., Zhou, Y., Qiu, L., and Zhang, J.: Quantifying the Uncertainties of China's Emission Inventory for Industrial Sources: From National to Provincial and City Scales, Atmospheric Environment, 165, 207–221, https://doi.org/10.1016/j.atmosenv.2017.06.045, 2017.